applied sciences

MDPI

Article

Numerical Investigation of Statistical Relationships Between Random Fiber Distributions and Mechanical Properties of Concrete Composites

Shihe Xiong [1], Zhenrui Zhou [1], Jiongyi Yan [2,*] and Yutai Su [1,*]

[1] School of Mechanics and Transportation Engineering, Northwestern Polytechnical University, Xi'an 710129, China
[2] Wolfson School of Mechanical Electrical and Manufacturing Engineering, Loughborough University, Loughborough LE11 3TU, UK
* Correspondence: j.j.yan@lboro.ac.uk (J.Y.); suyutai@nwpu.edu.cn (Y.S.)

Abstract

The mechanical behavior of fiber-reinforced concrete largely depends on the fiber morphology, geometry, and distribution. However, current numerical models do not take into account the stochastic properties of fibers with a spatial distribution, which limits their prediction accuracy and overlooks the critical impact of microstructural effects on macroscopic properties. To address this issue, a comprehensive numerical framework is developed using the Concrete Damage Plasticity (CDP) model for the concrete matrix, an elastoplastic model for steel fibers, and with cohesive zone elements applied to describe fiber–matrix interfacial debonding. Random fiber configurations are generated to represent statistical variability, and their effects on the elastic modulus, compressive strength, and tensile strength are systematically examined. A wide range of fiber parameters—including dimensions, volume fractions, stochastic orientation, and spatial distribution—is investigated to reveal microstructure-dependent mechanical behavior at the macroscale. The results highlight the critical roles of the fiber volume fraction and orientation control in enhancing mechanical behavior and provide practical guidelines for optimizing fiber incorporation strategies in concrete design.

Keywords: steel fiber-reinforced concrete; stochastic fiber distribution; Concrete Damage Plasticity; cohesive zone modeling; micromechanical simulation; tensile behavior; numerical simulation

check for updates

Academic Editor: Paulo Santos

Received: 18 November 2025
Revised: 6 December 2025
Accepted: 9 December 2025
Published: 16 December 2025

Citation: Xiong, S.; Zhou, Z.; Yan, J.; Su, Y. Numerical Investigation of Statistical Relationships Between Random Fiber Distributions and Mechanical Properties of Concrete Composites. *Appl. Sci.* **2025**, *15*, 13186. https://doi.org/10.3390/app152413186

Correction Statement: This article has been republished with a minor change. The change does not affect the scientific content of the article and further details are available within the backmatter of the website version of this article.

Copyright: © 2025 by the authors. Licensee MDPI, Basel, Switzerland. This article is an open access article distributed under the terms and conditions of the Creative Commons Attribution (CC BY) license (https://creativecommons.org/licenses/by/4.0/).

1. Introduction

Concrete, as the most common construction material, is long-established and widely used in various engineering applications [1]. However, pure concrete inherently exhibits low tensile strength and limited ductility. The incorporation of fibers—such as metallic, inorganic, organic, or plant-based fibers—into conventional concrete can effectively enhance its tensile, flexural, and compressive strengths, thereby improving the overall service performance of concrete structures [2,3]. This improvement is primarily attributed to the crack-bridging effect of the fibers. When cracks initiate, the fibers enable load transfer across the crack surfaces, enhancing the post-cracking ductility at the macroscopic scale, as shown in Figure 1. Owing to these superior mechanical properties, fiber-reinforced concrete (FRC) has attracted widespread attention in the construction industry [4].

Incorporating different types of fibers can significantly improve the mechanical properties and durability of concrete, including steel fibers, polypropylene fibers, basalt fibers, and hybrid fiber systems [5–13]. Studies on polypropylene fiber-reinforced concrete have shown that its tensile and flexural strengths are significantly improved, and its freeze–thaw resistance, permeability, and crack control are also enhanced under various loads and environmental conditions [5–8]. The compressive, tensile, fatigue, and freeze–thaw resistance of basalt fiber-reinforced concrete has been extensively studied, and it exhibits significant advantages under high-temperature exposure and freeze–thaw cycles [9–11]. Compared with single-fiber systems, hybrid fiber systems such as steel–polypropylene hybrid fiber systems and multi-fiber-reinforced concrete further demonstrate synergistic effects in toughness, post-cracking performance, and durability [12–14]. These experimental studies consistently demonstrate that the fiber type, volume fraction, geometry, and dispersion state have a significant impact on the macroscopic response of fiber-reinforced concrete.

Meanwhile, numerical and micromechanical modeling of fiber-reinforced concrete has also made rapid progress, with mesoscale and multiscale models developed to clearly characterize aggregates, fibers, and interfaces [15–18]. Three-dimensional fiber distributions generated by X-rays and statistics have been used to quantify the effects of the fiber orientation and spatial randomness on the stiffness, strength, and fracture behavior [15,16]. Advanced modeling strategies have also combined cohesive elements, damage-plasticity theory, and finite–discrete element combination techniques to capture crack initiation, propagation, and fiber-bridging mechanisms in steel fiber-reinforced concrete [18–20].

Nevertheless, the mechanical behavior of FRC depends on stochastic characteristics of the fibers at the microscale, including their distribution density, diameter, length, orientation, and spatial configuration [21–29]. In addition, the interfacial bonding between the fibers and the surrounding matrix plays a crucial role under loading, as it directly determines whether the fibers can effectively carry and transfer stress [25]. The inherent randomness of fiber characteristics, combined with the complex interfacial adhesion behavior, poses a significant challenge to accurately predicting the macroscopic mechanical properties of FRC, thereby hindering the reliable and optimized design of fiber-reinforced concrete structures.

Although experimental studies can provide valuable data and insights for material improvement, they are generally time-consuming and costly, and they exhibit significant limitations in investigating the stochastic nature of fiber distributions [26,27]. Moreover, experimental methods often struggle to accurately characterize the interfacial bonding behavior between fibers and the surrounding matrix [28]. Therefore, numerical simulation has become a powerful tool for elucidating the influence of complex internal structures on the mechanical performance of fiber-reinforced concrete. Previous studies have demonstrated the feasibility of numerical modeling of fiber-reinforced concrete. For example, Barros et al. applied a combined finite–discrete element method (FDEM) to simulate fracture propagation in FRC tunnels, yet acknowledged that fiber–matrix interfacial debonding was not fully resolved [29]. Landović et al. presented modeling of both small- and large-scale FRC girders, but identified major limitations in representing fiber spatial randomness and interface mechanics [30].

To this end, the present study establishes a comprehensive three-dimensional numerical framework to systematically analyze the effects of random fiber characteristics on the mechanical behavior of steel fiber-reinforced concrete. The Concrete Damage Plasticity (CDP) model is employed to capture the highly nonlinear response of the concrete matrix, including damage evolution under both compressive and tensile loading. In the model, steel fibers are represented using an elastic–plastic constitutive formulation, while the fiber–matrix interfacial interaction—encompassing debonding and pull-out mechanisms—is

explicitly modeled using cohesive elements. Table 1 shows comparisons between previous research and this study.

The core idea of the proposed method is to generate a large number of random fiber configurations within representative volume elements (RVEs), which explicitly account for the statistical variability of the fiber number, length, diameter, orientation, and spatial distribution. Based on that, this study aims to explore how this random fiber morphology and fiber–matrix interface behavior jointly determine the macroscopic mechanical response of steel fiber-reinforced concrete. Specifically, the objectives of this study are as follows:

1. To quantify the influence of random fiber parameters on the elastic modulus, compressive strength, and tensile strength of the composite material.
2. To establish a quantitative relationship between microstructural input variability and macroscopic mechanical properties through statistical analysis of simulation results.

The results emphasize that controlling the fiber number, length, diameter, orientation, and spatial distribution is crucial for achieving the desired structural performance and provides a micromechanical basis for optimizing fiber incorporation strategies and constructing a more reliable and performance-oriented design framework for fiber-reinforced concrete.

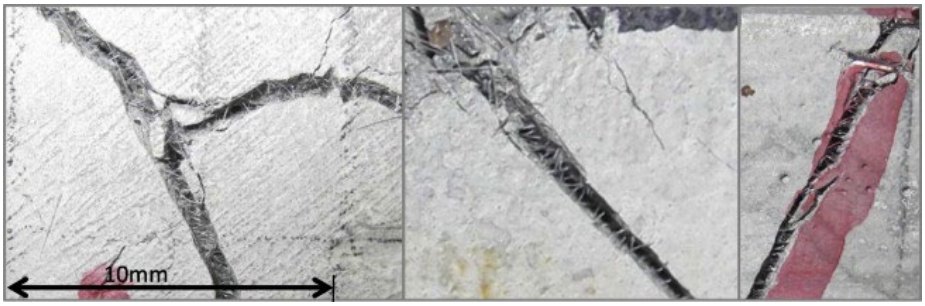


Figure 1. Fiber-bridging behavior of the ECC (engineered cementitious composite) panels after the impact [31].

Table 1. Comparison of different studies.

Study	Numerical Model and Loading Conditions	Treatment of Fiber Distribution and Stochasticity	Interfacial Modeling	Main Focus and Limitations Relative to the Present Work
Li et al. (2021) [15]	3D FE, CT-based SFRC members	Real CT field, no parametric study	Perfect bond (no cohesive)	Real fiber fields, without randomness and interface mechanisms
Naderi and Zhang (2022) [32]	3D meso FE, tension or compression	Some randomness, focus on fiber shape	Meso interface/damage, no fiber-wise cohesive	Fiber-shape and fracture, not RVE stochastic morphology
Li et al. (2020) [33]	3D meso SFRC analysis	Random with given volume fraction	Bond simplified/perfect	Global behavior, no separated random-parameter effects
Khalel and Khan (2023) [17]	Phenomenological regression model	Fiber inputs only, no explicit geometry	No explicit interface	Practical formulas, no microstructure–property mechanism
Kozák and Vala (2024) [20]	FEM with cohesive zones	Stochastic SFRC RVE not targeted	Cohesive cracks at structural scale	Cohesive concept, not CDP-based SFRC RVE
Present study	3D RVE FE, CDP and elastoplastic fibers	Controlled number/size/orientation/distribution	Explicit cohesive with damage, pull-out	Random morphology and interface damage lead to macroscopic strength

2. Model Description

2.1. Spatial Modeling and Overlap Detection

In the numerical simulation of fiber-reinforced composites, the first step involves constructing an appropriate spatial model within a finite 3D domain. The objective of spatial modeling is not merely to randomly distribute fibers within a cubic region, but to ensure that the resulting configuration reflects the statistical characteristics and spatial distribution patterns of fibers as observed in real materials.

The geometric characteristics of each fiber include its start point, end point, and diameter, which together define its fundamental shape and dimensions. Within a predefined spatial boundary, the centroid of each fiber is randomly generated, and its start and end points are subsequently determined according to the corresponding fiber length. The fiber orientation is assigned by random sampling from a uniform distribution of Euler angles, denoted as θ and φ, where θ represents the inclination angle relative to the positive z-axis in the Z direction (0–90°), and φ denotes the rotation angle within the xy-plane relative to the positive x-axis (0–360°). Both rotations conform to the right-handed Cartesian coordinate system. This approach enables the generation of a three-dimensional random fiber distribution. In addition, the fiber lengths are sampled from a uniform distribution within a specified range, ensuring geometric diversity while avoiding excessive uniformity that could otherwise reduce the representativeness of the model's overall mechanical response.

During the fiber placement process, a key issue that must be addressed is the spatial overlap between fibers, since they cannot occupy the same position or intersect without interfacial interaction. If such overlap occurs in the numerical model, it may lead to poor convergence or even failure of subsequent simulations. Hence, a new randomly generated fiber is excluded if the minimum distance between any two fibers is smaller than the average fiber diameter of them. In this case, this fiber is discarded and regenerated to ensure the validity of the model.

This overlap detection procedure serves not only as a geometric constraint but also plays an important role from a mechanical perspective. Thanks to this detection and filtering strategy, the final fiber distribution more closely conforms to realistic physical laws and provides a defect-free initial configuration for subsequent finite element analysis.

The characteristic information of each fiber is ultimately defined by four sets of parameters: its start point, end point, diameter, and orientation angles, combined with the overlap detection process. In this way, every fiber can be uniquely determined within the given three-dimensional domain, thereby providing a reliable foundation for subsequent mesh generation and finite element analysis.

2.2. Material Properties and Interaction Behaviors

The definition of material properties and the specification of interaction behaviors between the matrix and fibers are crucial steps in the present numerical modeling, as they determine which mechanical factors need to be considered to ensure consistency with experimental observations. In the developed model, both the fibers and the concrete matrix are explicitly defined with their respective material properties. The model of steel fiber is characterized by an elastoplastic model, and the corresponding parameters are illustrated in Table 2. For the concrete matrix, both the elastic modulus and Poisson's ratio are assigned, and the CDP model is employed to capture the nonlinear tensile behavior and damage evolution of concrete under loading; the corresponding parameters are illustrated in Table 3.

Table 2. Material parameters of the fibers [34].

Elastic		Plastic	
Young's Modulus	**Poisson's Ratio**	**Yield Stress**	**Plastic Strain**
206,000	0.3	235	0
		345	0.005
		400	0.015
		450	0.05
		480	0.1

Table 3. Material parameters of the matrix [35,36].

Elastic		Concrete Damage Plasticity										
		Plasticity					Compressive Behavior			Tensile Behavior		
Young's Modulus	**Poisson's Ratio**	**Dilation Angle**	**Eccentricity**	**fb0/fc0**	**k**	**Viscosity Parameter**	**Yield Stress**	**Inelastic Strain ($\times 10^{-3}$)**	**Damage Parameter**	**Yield Stress**	**Cracking Strain ($\times 10^{-3}$)**	**Damage Parameter**
300	0.2	15	0.1	1.16	0.667	0.001	15.45	0	0.000	2.01	0	0.000
							18.48	0.151	0.065	0.66	0.35	0.359
							19.93	0.376	0.137	0.419	0.647	0.620
							20.1	0.515	0.178	0.319	0.937	0.756
							19.61	0.833	0.264	0.226	1.513	0.876
							15.88	1.893	0.501	0.18	2.087	0.924
							12.49	2.937	0.665	0.152	2.66	0.949
							10.07	3.934	0.767	0.13	3.327	0.964
							7.5	5.528	0.861			
							4.89	8.995	0.939			

Furthermore, a cohesive contact interface is established between the concrete matrix and the embedded steel fibers to simulate interfacial cracking, damage, and debonding processes. The incorporation of the cohesive interface enables the model to realistically reproduce the bridging effect of fibers across crack surfaces, thereby reflecting the actual crack propagation behavior observed in fiber-reinforced concrete. The corresponding parameters are illustrated in Table 4.

Table 4. Cohesive interface damage parameters [37,38].

Cohesive Behavior			Damage					
			Initiation			Evolution		
Knn	**Kss**	**Ktt**	**Normal Only**	**Shear-1 Only**	**Shear-2 Only**	**Normal Fracture Energy**	**1st Shear Fracture Energy**	**2nd Shear Fracture Energy**
10,000	10,000	10,000	60	80	80	0.6	2.1	2.1

2.3. Modelling Scale and Homogenization Assumptions

In a rigorous sense, filler concrete is a heterogeneous system that may require coupled macro–meso–micro analyses using advanced multiscale homogenization techniques [39].

This study only constructed a mesoscale numerical framework. The concrete matrix within RVEs is described using a homogenized CDP model, while the steel fibers and fiber–matrix interfaces are explicitly represented using elastoplastic constitutive relations and cohesive zone elements, respectively. Therefore, the microscopic heterogeneity of the cement paste and interfacial transition zone (ITZ) is not analyzed through individual particles or pores, but rather contained within the given CDP and cohesive parameters.

Then, the macroscopic response of steel fiber-reinforced concrete is obtained by homogenizing the reaction forces at the RVE boundaries under a given uniaxial tension and interpreting the mean stress–strain curve as effective stiffness and tensile strength. In

this sense, this study employs a homogenization strategy from mesoscale to macroscale, rather than a fully coupled three-scale (macro–meso–micro) framework. This study does not directly transfer the original parameters from the microscale to the structural scale one-to-one; instead, it first gives the CDP and interface parameters at the material level and then uses them for mesoscale RVE analysis. While more complex multi-scale schemes (such as FE^2 or adaptive RVE coupling) are available for concrete and other heterogeneous materials, this study focuses on quantifying the sensitivity of macroscopic tensile behavior to random fiber morphology and interfacial debonding within a statistically representative mesoscale volume.

3. Constitutive Modeling

The constitutive modeling in this study consists of three components: the fiber constitutive model, the CDP constitutive model, and the fiber–matrix interface constitutive model.

3.1. Fiber Constitutive Model

The fiber material in the constitutive model is steel, and its deformation behavior can be adequately represented using a relatively simple elastic–plastic constitutive model.

3.1.1. Elastic Stage

In the elastic stage, the steel fibers follow Hooke's law, and their anisotropic stress–strain relationship can be expressed in the following matrix form:

$$\begin{bmatrix} \sigma_1 \\ \sigma_2 \\ \sigma_3 \\ \tau_{12} \\ \tau_{13} \\ \tau_{23} \end{bmatrix} = \begin{bmatrix} E_1 & \nu_{12}E_2 & \nu_{13}E_3 & 0 & 0 & 0 \\ \nu_{12}E_1 & E_2 & \nu_{23}E_3 & 0 & 0 & 0 \\ \nu_{13}E_1 & \nu_{23}E_2 & E_3 & 0 & 0 & 0 \\ 0 & 0 & 0 & G_{12} & 0 & 0 \\ 0 & 0 & 0 & 0 & G_{13} & 0 \\ 0 & 0 & 0 & 0 & 0 & G_{23} \end{bmatrix} \begin{bmatrix} \varepsilon_1 \\ \varepsilon_2 \\ \varepsilon_3 \\ \gamma_{12} \\ \gamma_{13} \\ \gamma_{23} \end{bmatrix} \quad (1)$$

where E is Young's modulus, G is the shear modulus, σ and ε denote the components of stress and strain, respectively, τ represents the shear stress, γ represents the shear strain, and ν is Poisson's ratio. The subscripts 1, 2, and 3 correspond to the fiber axial direction and the two mutually perpendicular transverse directions.

3.1.2. Plastic Stage

In the plastic stage, a power-law constitutive model can be employed:

$$\sigma = K \cdot \varepsilon^n \quad (2)$$

where σ denotes the material stress, ε represents the plastic strain, K is the hardening coefficient, and n is the hardening exponent.

The coefficient K is closely related to the material's yield strength. In certain steels, a higher yield strength generally corresponds to a larger value of K. The hardening exponent n is typically relatively small, as the plastic hardening behavior of steel is gradual, though still nonlinear. Both K and n usually need to be determined by fitting to experimental data, and therefore they exhibit a degree of dependence on experimental characterization.

3.2. Constitutive Model Based on the CDP Model

The CDP model is widely used in finite element analysis to simulate the nonlinear behavior of concrete under complex loading conditions, including cracking, damage, and failure [40]. It combines plasticity theory and damage mechanics to account for both the

material's ability to undergo inelastic deformation and the degradation of its strength [41]. In this work, although steel fibers are incorporated into the concrete matrix, the constitutive behavior is still represented using the isotropic CDP framework. The presence of fibers is reflected through modified material parameters rather than altering the fundamental formulation of the CDP model, consistent with a modified plastic damage model for steel fiber-reinforced concrete.

3.2.1. Elastic Stage

In the elastic stage of the CDP model, the stress–strain response of concrete follows Hooke's law, with the ratio between stress and strain determined by the elastic modulus.

The constitutive equation can be written as

$$\sigma = \mathbf{D} : \epsilon \tag{3}$$

where σ is the stress tensor, which contains the individual stress components, $\mathbf{D}$ is the damage-modified stiffness tensor, which depends on the elastic modulus and the damage variables of the material, and ϵ is the strain tensor, which contains the individual strain components.

The damage-modified stiffness matrix can be expressed as

$$\mathbf{D} = \mathbf{D}_0(1 - D) \tag{4}$$

where $\mathbf{D}_0$ denotes the stiffness matrix of the undamaged material, which represents the elastic properties prior to the onset of damage, D is the damage variable, which represents the degree of material degradation, and the stiffness of the material progressively decreases as damage evolves.

3.2.2. Plastic Stage

When the stress in concrete exceeds its yield strength, the material enters the plastic stage. The CDP model employs the von Mises yield criterion to describe the plastic behavior of concrete under both compressive and tensile loading. The yield criterion for concrete can be expressed as

$$f(\sigma) = \sigma_{eq} - \sigma_{yield} = 0 \tag{5}$$

where σ_{eq} denotes the equivalent stress, which is associated with the stress state and the plastic deformation of the concrete, and σ_{yield} represents the yield strength, which defines the critical stress at which concrete transitions from the elastic stage to the plastic stage.

The damage variable reflects the extent of material degradation under various stress states. In the CDP model, the evolution of the damage variable D changes continuously during loading, and its development is related to the plastic strain and the stress state. The damage evolution function typically takes the following form:

$$D = D\left(\epsilon_{pl}\right) \tag{6}$$

where D represents the damage variable, and ϵ_{pl} represents the plastic strain, which indicates the irreversible deformation of the concrete material during loading.

By combining elastic behavior, plastic deformation, and damage evolution, the constitutive equation of the CDP model can be expressed in the following form:

$$\sigma = \mathbf{D}_0(1 - D) \ : \ \epsilon_{total} \tag{7}$$

where $\mathbf{D}_0$ represents the stiffness matrix of the undamaged material, D represents the damage variable, which increases progressively as loading and damage develop in the concrete, and ϵ_{total} represents the total strain, which consists of both elastic and plastic components.

3.3. Cohesive Interface Model

The cohesive contact constitutive model is a numerical approach used to simulate the processes of cracking, damage, and fracture at material interfaces [42]. Its core principle lies in describing the progressive degradation of the interface from initial bonding to complete failure through a nonlinear damage variable, typically represented by damage strain or fracture energy. The model generally assumes that, in the initial loading stage, the interface can transmit both normal and tangential stresses. When the applied normal tensile stress or tangential shear stress exceeds a critical threshold, microcracks or localized plastic deformation begin to develop, leading the interface to gradually enter the failure stage [43].

The constitutive relationship can be expressed as

$$\sigma_n = \sigma_n(\delta_n) \tag{8}$$

$$\sigma_t = \sigma_t(\delta_t) \tag{9}$$

where σ_n represents the normal traction, σ_t represents the shear traction, δ_n and δ_t denote the normal and tangential displacements, respectively.

These relationships are expressed through a nonlinear damage evolution function that relates the interface displacement to the damage variable. Typically, the evolution of interface damage is governed by the critical fracture energy G_c. The relationship between interface damage and crack propagation is described by the following damage evolution law:

$$G = \int_0^{\delta} \sigma(\delta) d\delta \tag{10}$$

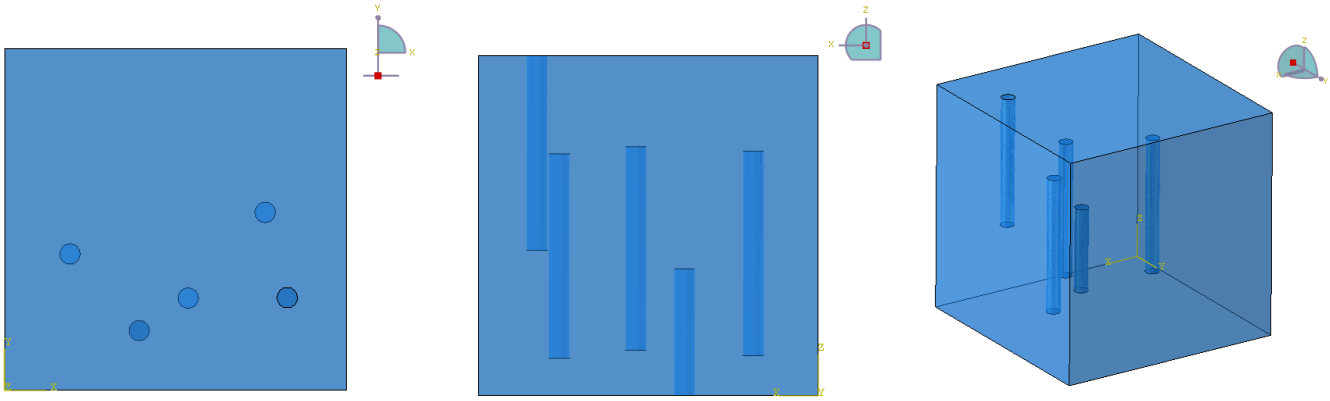
where G denotes the fracture energy, which represents the energy required for crack propagation along the interface, $\sigma(\delta)$ represents the stress associated with the interface separation displacement, and δ denotes the interface separation displacement.

When the total fracture energy accumulated during crack propagation reaches the critical value G_c, complete interface failure occurs.

4. Mechanical Simulation of Random FRC Models

In the modeling process, the method of controlling variables is adopted to separate and identify each parameter's effect on macroscopic mechanical properties of FRC. A fiber-reinforced concrete model with a specific set of parameters is selected as the reference model. The concrete block is a cube with a side length of 1 mm, composed of C20 concrete. Five fibers are embedded inside the block, made of Q235 steel. Each fiber has a diameter of 0.06 mm and a nominal length of 0.6 mm. Due to the random spatial fiber placement, some fibers may be partially truncated by the boundaries of the block, resulting in fiber ends exposed on the surface, whereas untruncated fibers remain fully embedded within the matrix. The fiber orientation is aligned with the tensile loading direction (for simplification, the orientation angles θ and φ of all fibers are both set to 0). The spatial distribution pattern of fibers is determined by the eigenvalues in the code. A fixed eigenvalue corresponds to a specific distribution configuration, and this eigenvalue is only the model's corresponding number and is not used as any model parameter. For example, Model-1010 corresponds to the reference model, where 1010 is the eigenvalue of that model. By varying five key parameters individually and comparing each modified model to the reference model, the

influence of microstructural fiber characteristics on the macroscopic mechanical response is investigated. The reference model Model-1010 is shown in Figure 2.



(**a**) (**b**) (**c**)

Figure 2. (**a**) Z-axis view, (**b**) X-axis view, and (**c**) oblique view of the reference fiber-reinforced concrete model.

Loads and boundary conditions are shown in Figure 3. Monotonic, displacement-controlled uniaxial tension is applied on the top face along the z-direction, while the bottom face is fixed in the z-direction. The prescribed vertical displacement increases linearly with the analysis time from $u_z = 0$ to $u_z = U_{max} = 0.1$ over a total step time $T_{end} = 0.1$. The resulting nominal axial strain rate in the normalised analysis time is

$$\dot{\varepsilon}_{zz} = \frac{U_{\max}}{L_0\, T_{\text{end}}} = \frac{0.1}{1.0 \times 0.1} = 1.0\ \text{s}^{-1}. \tag{11}$$

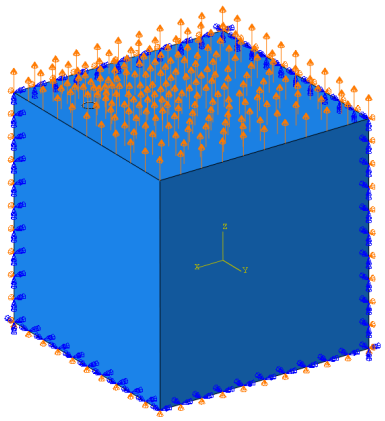


Figure 3. Loading condition (tensile load applied on the top surface).

In the Abaqus input file (Abaqus 2021 software, version 6.21-1), this loading is implemented as a time-dependent boundary condition on all nodes of the top surface,

$$u_z(t) = U_{\max}\, A(t), \tag{12}$$

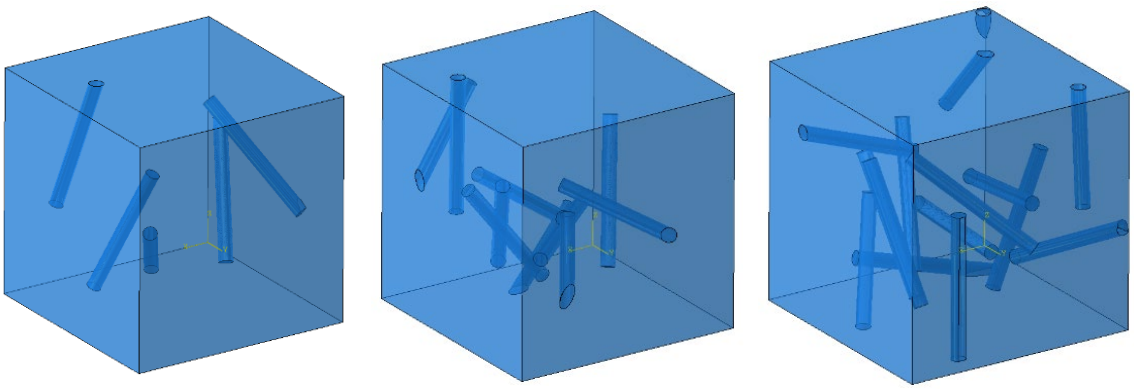
where $A(t)$ is a user-defined amplitude varying linearly from 0 to 1 between $t = 0$ and $t = T_{\text{end}}$. A static general step with displacement control is used.

The analysis time is treated as pseudo-time, and the solution corresponds to a quasi-static equilibrium path. The selected displacement-controlled loading method is consistent with the standard quasi-static direct tensile test type for fiber-reinforced concrete, and

the RILEM TC 162-TDF recommendation for uniaxial tensile testing specifies low-rate displacement control [44].

4.1. Different Numbers of Fibers

As shown in Figure 4, the number of fibers is varied from 2 to 17, resulting in 16 fiber configurations, and the spatial distributions of the fibers do not overlap. In this section, the truncation of fibers caused by random placement near the boundaries of the concrete block is not considered when the number of fibers increases. The configuration with five fibers corresponds to the reference model. This part of the study focuses on examining the effect of an increasing fiber quantity on the uniaxial tensile behavior of the concrete block, while neglecting the influence of fiber length reduction due to boundary truncation.

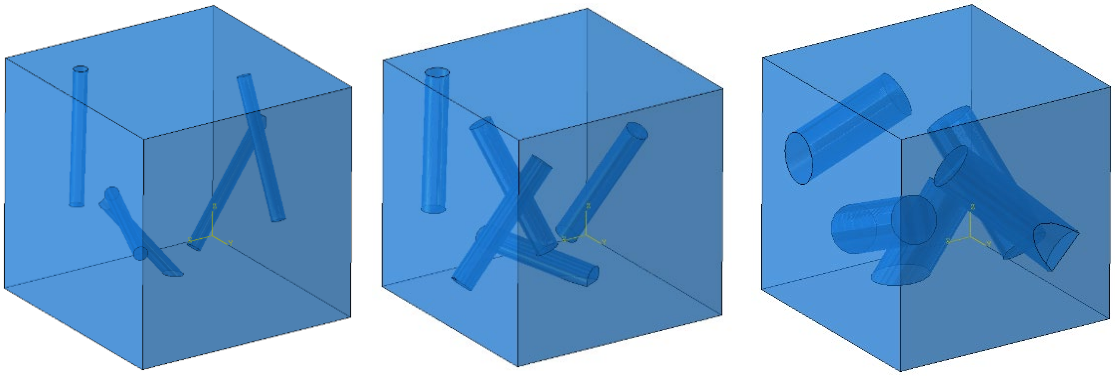


(**a**) (**b**) (**c**)

Figure 4. Oblique views of models with (**a**) 5, (**b**) 10, and (**c**) 15 fibers.

4.2. Different Fiber Diameters

As shown in Figure 5, the fiber diameter is varied from 0.05 mm to 0.1 mm, with increments of 0.005 mm, resulting in 11 different diameter configurations, where a diameter of 0.06 mm corresponds to the reference model. As the fiber diameter increases, the spatial distribution of the fibers remains non-overlapping.



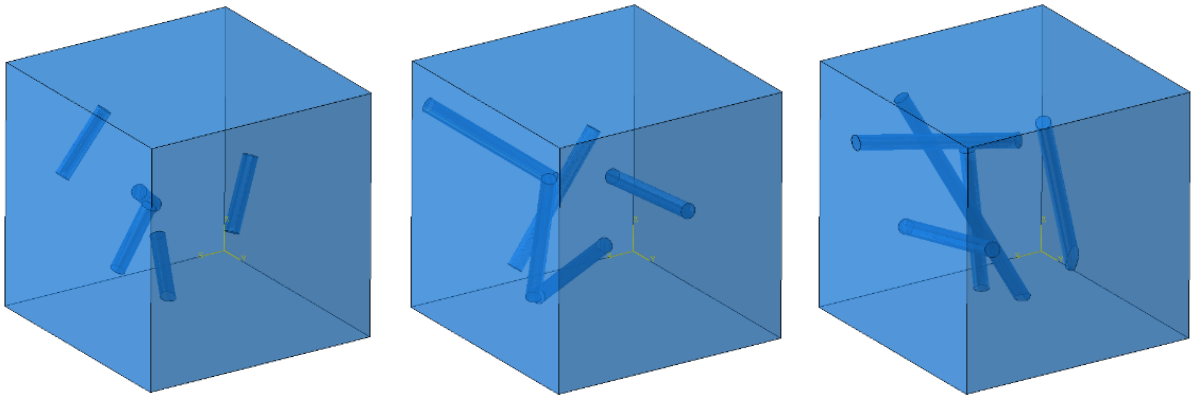
(**a**) (**b**) (**c**)

Figure 5. Oblique views of models with fiber diameters of (**a**) 0.06 mm, (**b**) 0.1 mm, and (**c**) 0.2 mm.

4.3. Different Fiber Lengths

As shown in Figure 6, the fiber length is varied from 0.2 mm to 1.0 mm, with increments of 0.05 mm, resulting in 17 length configurations, where a length of 0.6 mm corresponds to the reference model. Due to the random spatial distribution of fibers within the concrete block, shorter fibers are fully embedded within the matrix, whereas longer fibers may be partially truncated by the block boundaries. This section focuses primarily on analyzing

the influence of the dominant fiber length on the uniaxial tensile behavior of the concrete block, while neglecting the effect of length reduction caused by fiber truncation.

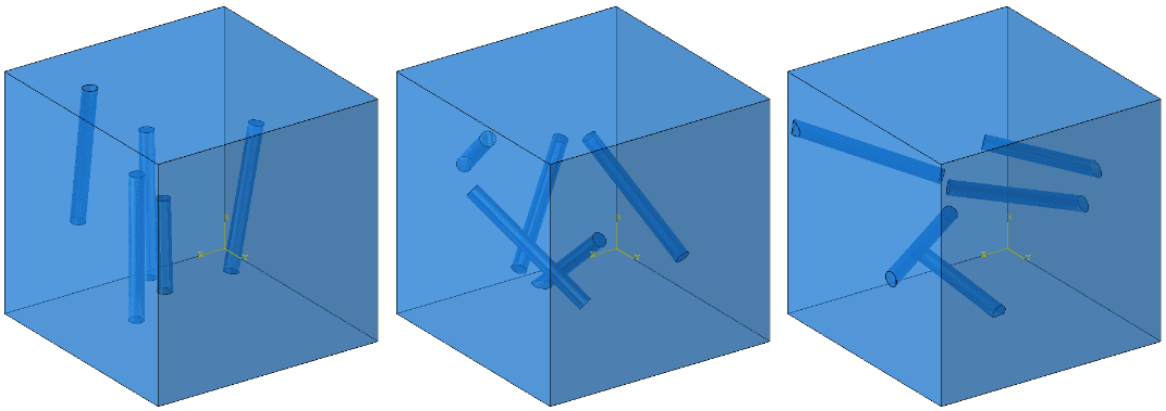


(**a**) (**b**) (**c**)

Figure 6. Oblique views of models with fiber lengths of (**a**) 0.3 mm, (**b**) 0.6 mm, and (**c**) 1.0 mm.

4.4. Different Fiber Orientations

As shown in Figure 7, the fiber orientation is defined using two angles, θ and φ. The range of θ is divided into six intervals: 0–15, 15–30, 30–45, 45–60, 60–75, and 75–90 degrees, with three samples selected per interval, resulting in a total of 18 configurations. The φ parameter is assigned over the full range of 0–360 degrees. Both θ and φ are randomly selected within their respective intervals using a random function, which aligns with practical engineering conditions. The models are numbered from 1 to 18 accordingly: models 1–3 correspond to the range 0–15°, 4–6 to 15–30°, 7–9 to 30–45°, 10–12 to 45–60°, 13–15 to 60–75°, and 16–18 to 75–90°.

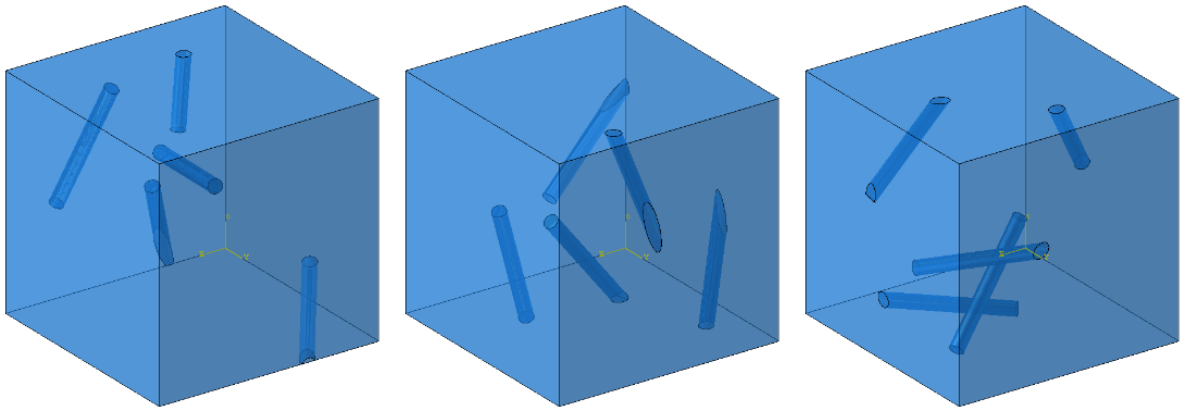


(**a**) (**b**) (**c**)

Figure 7. Oblique views of models with fiber orientation angles ranging at (**a**) 0–15°, (**b**) 45–60°, and (**c**) 75–90°.

4.5. Different Spatial Distributions of Fibers

As shown in Figure 8, the spatial distribution of fibers in the simulation is determined by the eigenvalues, which range from 1010 to 1029. Due to the geometric complexity and severe mesh distortion of certain configurations, several models (specifically 1022, 1024, 1027, and 1028) failed to converge and were therefore discarded. A total of sixteen valid configurations remain, with the model labeled with an eigenvalue of 1010 defined as the reference configuration.



(a) (b) (c)

Figure 8. Oblique view of the model with fiber eigenvalues of (**a**) 1020, (**b**) 1030, and (**c**) 1040.

4.6. Definition of the Ultimate Limit State Under Uniaxial Tension

For all simulations, the RVE is subjected to monotonically increasing, displacement-controlled uniaxial tension along the z-direction. The nominal axial stress $\sigma_{zz}(t)$ and average axial strain $\varepsilon_{zz}(t)$ are computed as

$$\sigma_{zz}(t) = \frac{F_{zz}(t)}{A_{\text{top}}} = \frac{\sum_i RF3_i(t)}{A_{\text{top}}}, \quad \varepsilon_{zz}(t) = \frac{u_z(t)}{L_0}, \tag{13}$$

where $F_{zz}(t)$ is the sum of the reaction forces in the loading direction on the top face, A_{top} is the area of the loaded face, $u_z(t)$ is the prescribed displacement in the z-direction, and L_0 is the initial specimen height.

The effective tensile strength of the fiber-reinforced concrete at the RVE level is defined as the peak value of the nominal stress–strain response, i.e.,

$$f_{t,\text{eff}} = \max_t \sigma_{zz}(t). \tag{14}$$

The ultimate limit state under uniaxial tension is reached when the nominal axial stress attains this maximum, after which stiffness degradation and loss of load-carrying capacity occur due to matrix cracking and fiber–matrix interfacial debonding.

In the classical limit-state form, the ultimate state function can be written as

$$g = R - S, \tag{15}$$

where R is the tensile resistance and S is the effect of actions. In the present study, at the RVE level, we have

$$R = f_{t,\text{eff}}, \quad S = \sigma_{zz}, \tag{16}$$

so that failure (ultimate limit state) occurs when

$$g = f_{t,\text{eff}} - \sigma_{zz} \leq 0. \tag{17}$$

This definition is used consistently to compare the ultimate tensile behavior of different stochastic fiber configurations.

5. Results and Discussion

For the purpose of analysis and to simplify the evaluation metrics, the post-processing considers the reaction force component in the positive z-direction on the top surface as the effective tensile stress. The simulation results of the reference model are shown in Figure 9.

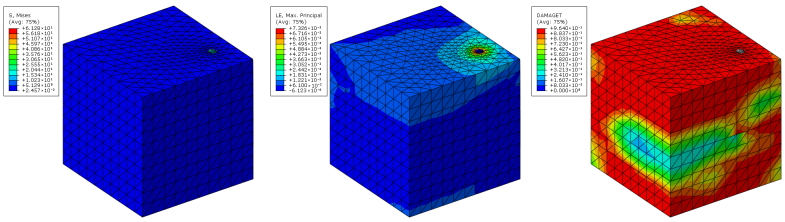
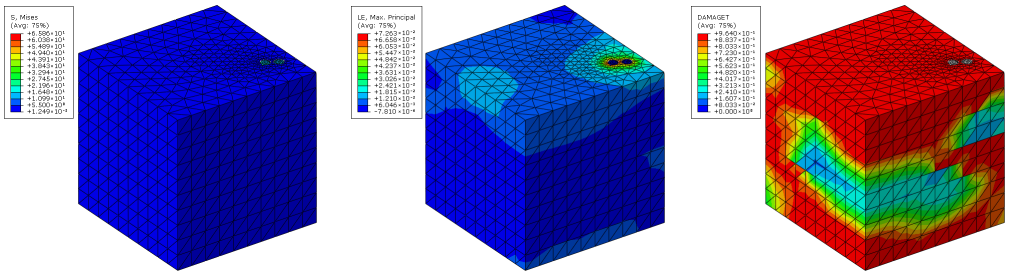


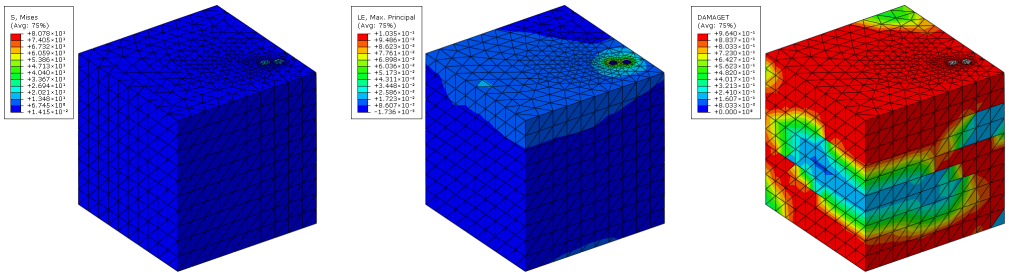
Figure 9. (**a**) von Mises stress, (**b**) maximum principal strain, and (**c**) damage of the reference model.

5.1. Effect of Fiber Quantity on the Mechanical Behavior

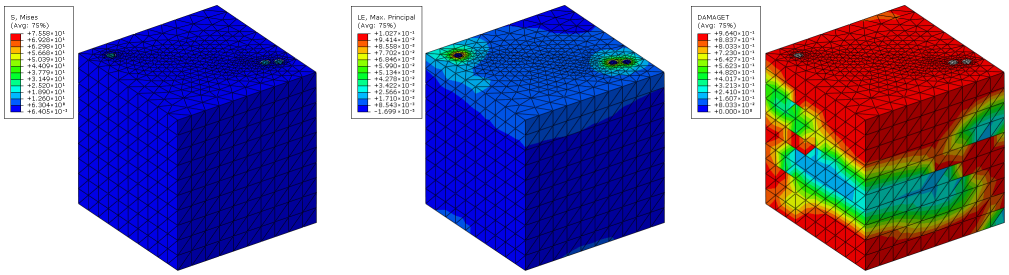
Analysis of the simulation results and stress–strain curves shown in Figures 10 and 11 reveals that the stress in all groups gradually increases during tensile loading, then rapidly decreases after reaching their respective peak values. Increasing the fiber count significantly improves the overall strength of the specimen when the fiber count is low.



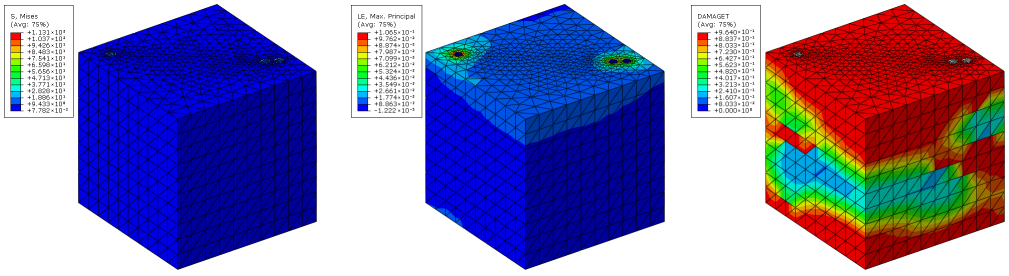
(**a**) The number of fibers is 8.



(**b**) The number of fibers is 11.



(**c**) The number of fibers is 14.



(**d**) The number of fibers is 17.

Figure 10. von Mises stress, maximum principal strain, and damage in models with different numbers of fibers.

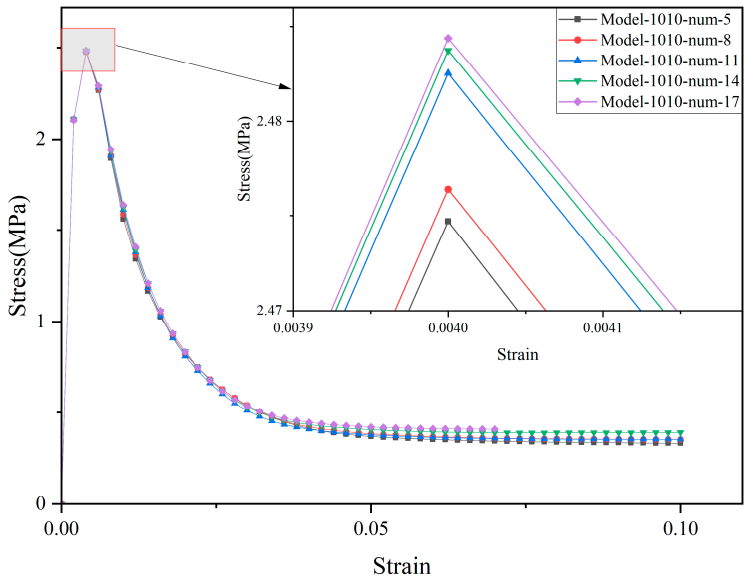


Figure 11. Stress–strain curves of models with different numbers of fibers.

As shown in Figure 12, the maximum stress generally increases with an increasing fiber count. However, when the fiber count reaches 17, the maximum stress decreases. This phenomenon is attributed to the random spatial distribution of fibers in the simulation—when fibers are unevenly aggregated in the matrix, local "dense regions" and "void regions" are formed, disrupting the continuity of the load transfer chain. Consequently, microcracks initiate prematurely, leading to a decrease or fluctuation in the maximum stress. The initial Young's modulus exhibits a non-monotonic change with an increasing fiber count, showing a continuous decrease in some ranges, while suddenly increasing at fiber counts of 3 and 10. This fluctuation is mainly related to the difference in the random distribution and orientation of fibers in the RVE. When the added fibers appear in the fiber vacancy area, the initial Young's modulus will increase significantly. However, when the increase in fibers aggravates the aggregation phenomenon, the initial Young's modulus will continue to decrease.

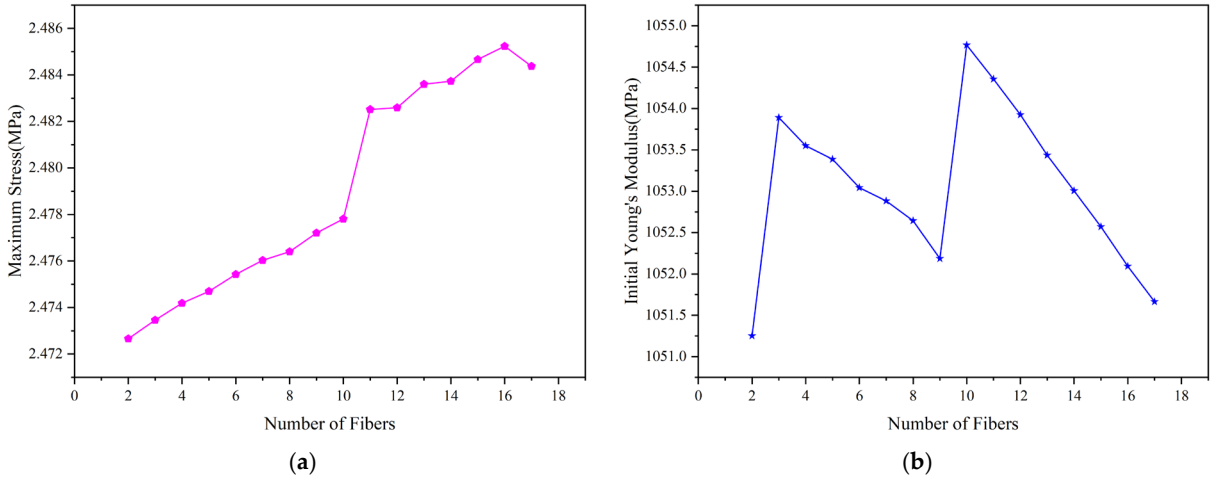


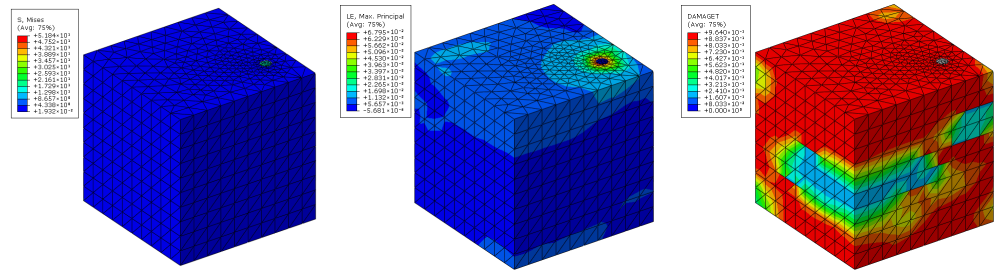
Figure 12. The effect of different fiber numbers on (**a**) maximum stress and (**b**) initial Young's modulus.

According to the experimental study by Luo et al. [45] on C20 steel fiber-reinforced concrete under intermediate strain rates, the splitting tensile strength of SFRC with a steel fiber volume fraction of 1% reaches about 2.96 MPa. In the present numerical model, the corresponding tensile strength obtained for C20 concrete with 1% Q235 steel fibers

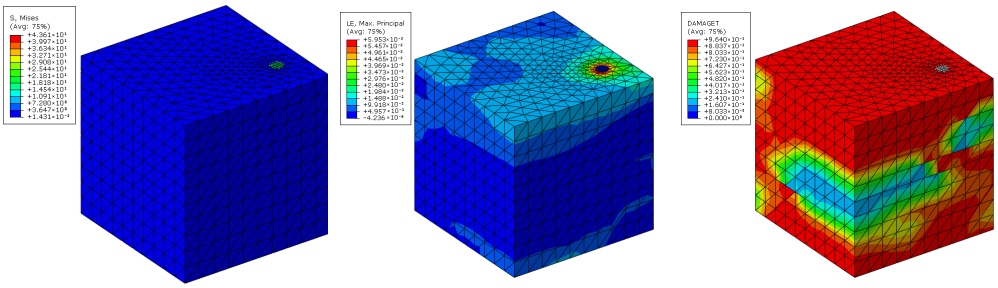
is 2.48 MPa, which is in good agreement with Luo's experimental result. The relative error between the simulation and the test data is $(2.96 - 2.48)/2.96 \times 100\% \approx 16.2\%$, indicating that the proposed mesoscale model can reasonably capture the tensile resistance of low-strength SFRC with a 1% steel fiber volume fraction.

5.2. Effect of Fiber Diameter on the Macroscopic Mechanical Behavior

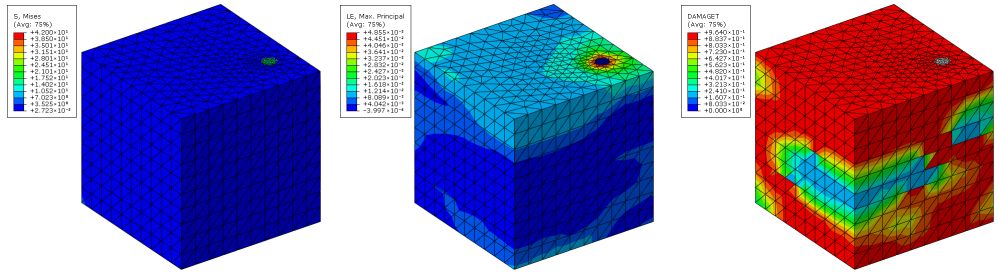
As shown in Figures 13 and 14, both the maximum tensile stress and the initial Young's modulus decrease monotonically with an increasing fiber diameter in the investigated range. Specimens with a fiber diameter of 0.050 mm exhibit the highest tensile stress, and further enlargement of the diameter leads to a gradual reduction in tensile capacity. Similarly, the initial Young's modulus continuously decreases as the fiber diameter increases, as illustrated in Figure 15.



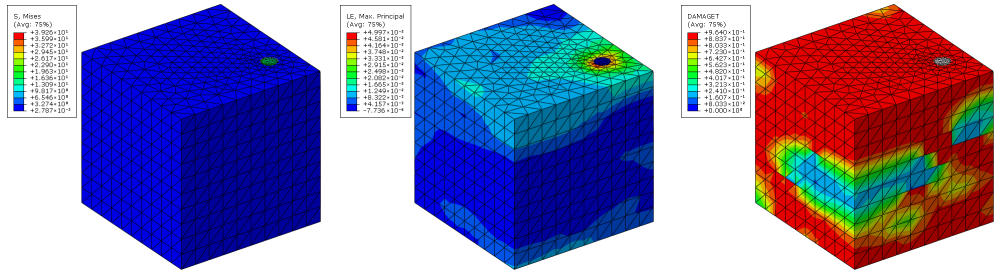
(**a**) The diameter of each fiber is 0.07.



(**b**) The diameter of each fiber is 0.08.



(**c**) The diameter of each fiber is 0.09.



(**d**) The diameter of each fiber is 0.10.

Figure 13. von Mises stress, maximum principal strain, and damage for models with different fiber diameters.

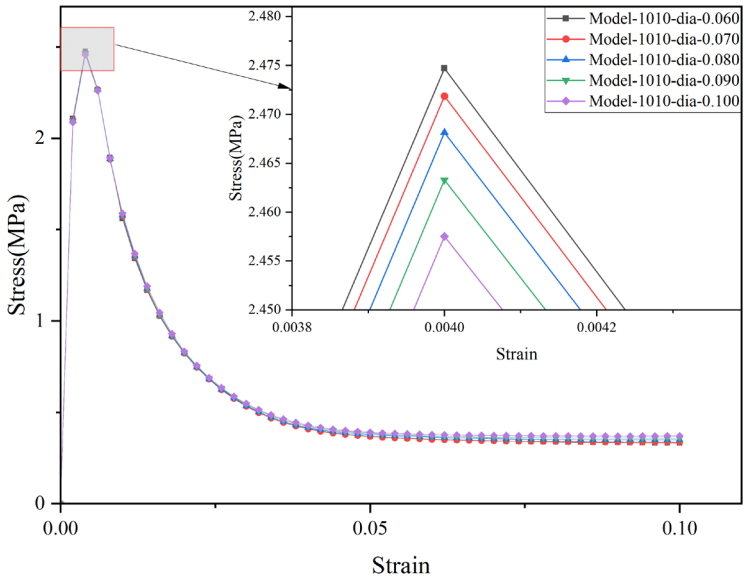
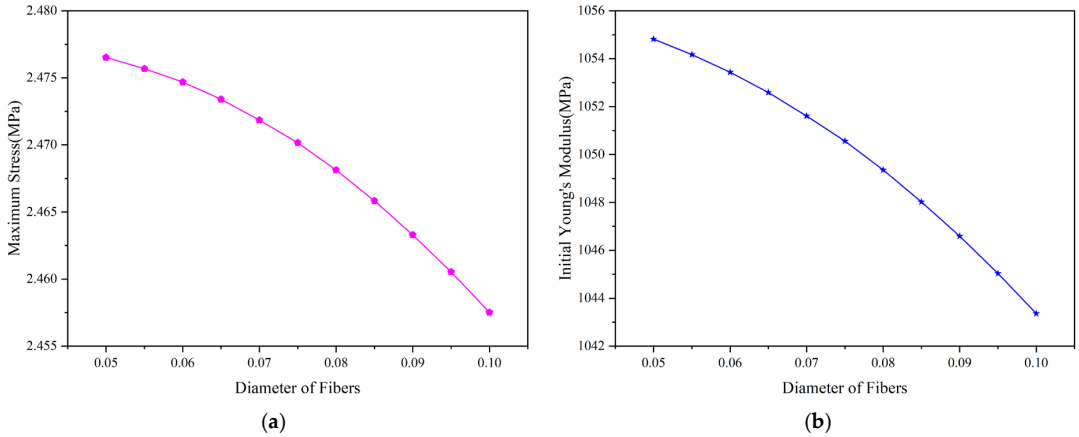


Figure 14. Stress–strain curves of models with different diameters of fibers.



(**a**) (**b**)

Figure 15. The effect of different fiber diameters on (**a**) maximum stress and (**b**) initial Young's modulus.

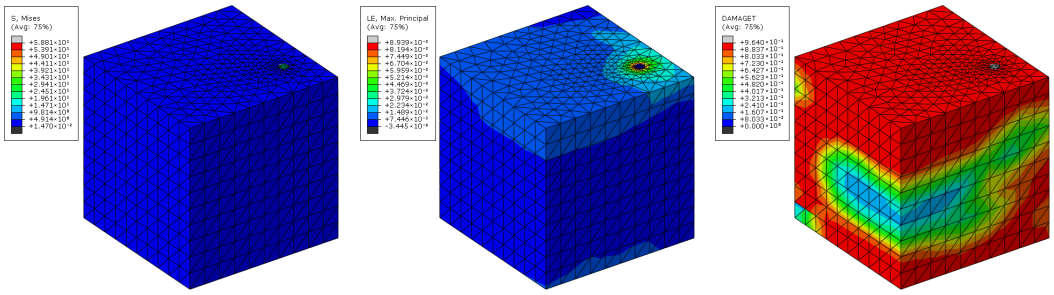
This trend can be interpreted in terms of three competing mechanisms: the steel-phase volume fraction, the minimum matrix gap S_{min} between adjacent fibers, and debonding of the cohesive interface. Although a larger fiber diameter increases the steel-phase volume fraction, it simultaneously reduces S_{min}, resulting in thinner matrix ligaments and more pronounced stress concentration around the interfaces. The reduced ligament thickness promotes earlier initiation and propagation of interface damage, which impairs the efficiency of load transfer from the matrix to the fibers. Within the present diameter range, the detrimental effects of matrix gap reduction and interface debonding dominate over the beneficial contribution of the increased steel-phase volume fraction, leading to a net decrease in both tensile strength and initial Young's modulus.

5.3. Effect of Fiber Length on the Macroscopic Mechanical Behavior

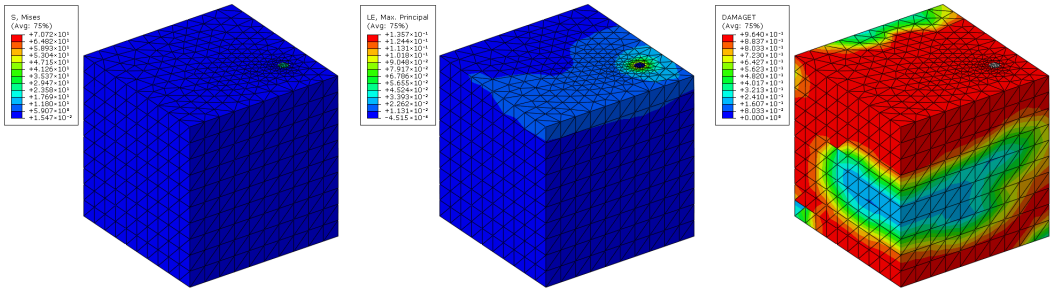
As shown in Figures 16 and 17, the tensile strength of the specimen increases with an increasing fiber length. Within the length range considered in this study, the fiber length has a significant influence on the tensile strength of the specimen. The effect reaches its maximum when the fiber length is approximately 0.45, while both shorter and longer fibers exhibit a reduced influence on the overall tensile performance.

The analysis of the stress with respect to the fiber length, shown in Figure 18, shows an overall increasing trend, with a faster growth rate in the mid-range and slower variations at

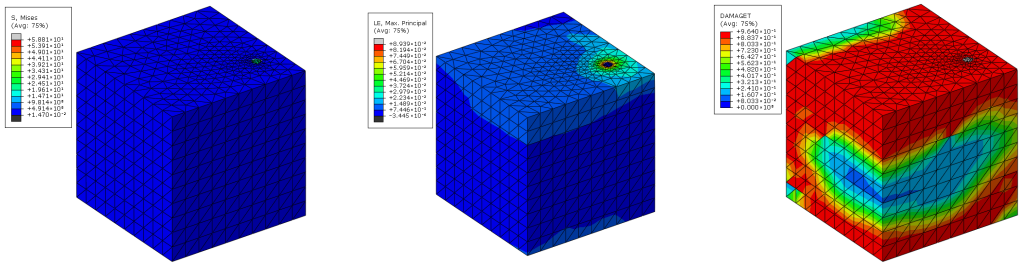
both ends, which is consistent with the conclusions drawn previously. In the analysis of the initial Young's modulus as a function of fiber length, shown in Figure 18, a nonlinear trend can be observed: the modulus first decreases and then increases as the fiber length increases. This behavior can be explained by the existence of a critical fiber length (l_c). When the fiber length is shorter than this critical value, the interfacial shear transfer is insufficient, where the fibers are not long enough to participate in load bearing and potentially create numerous localized stress concentration, which leads to a slight reduction in the equivalent stiffness. Once the fiber length exceeds the critical length, the fibers gradually develop their full load-carrying capacity, resulting in a continuous increase in the overall modulus and a marked enhancement of the mechanical stiffness.



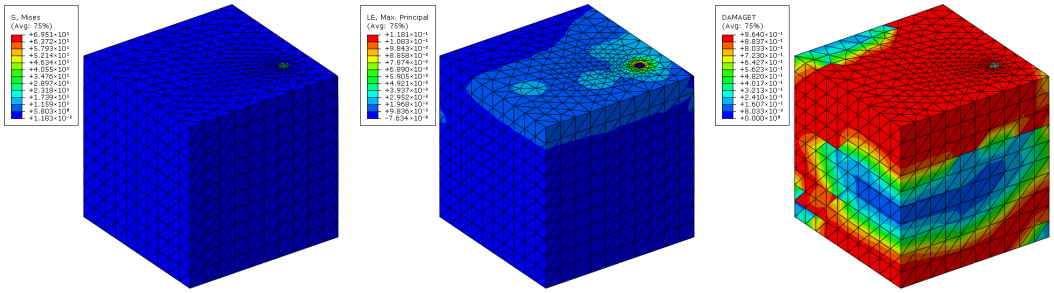
(**a**) The fiber length is 0.7.



(**b**) The fiber length is 0.8.



(**c**) The fiber length is 0.9.



(**d**) The fiber length is 1.0.

Figure 16. von Mises stress, maximum principal strain, and damage for models with different fiber lengths.

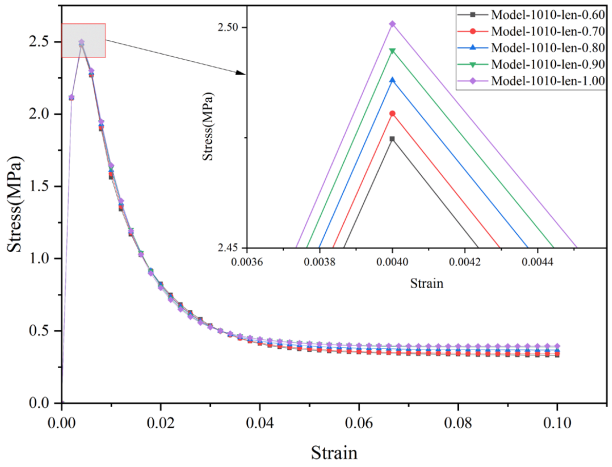
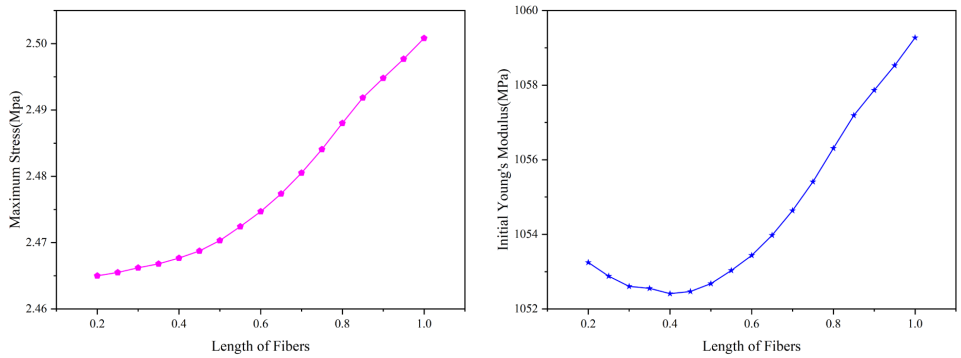


Figure 17. Stress–strain curves of models with different lengths of fibers.



(**a**) (**b**)

Figure 18. The effect of different fiber lengths on (**a**) maximum stress and (**b**) initial Young's modulus.

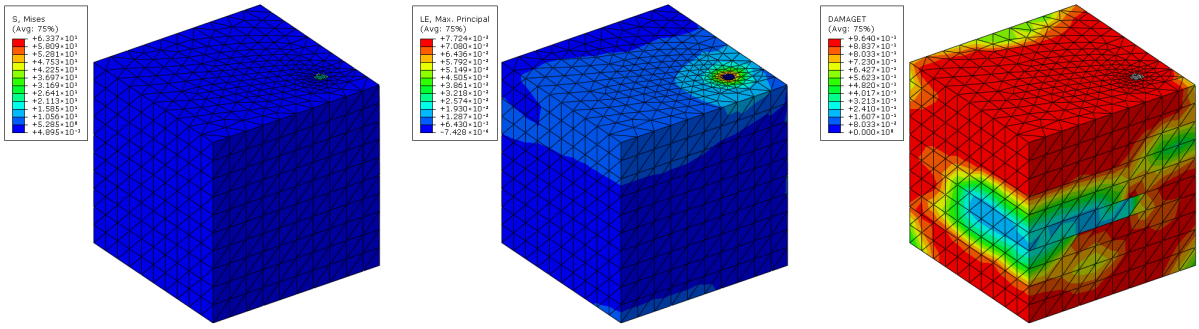
5.4. Effect of Fiber Orientation on the Macroscopic Mechanical Behavior

Since the five fibers in each model are randomly generated within the specified range, the average values of θ and φ for the five fibers are calculated and used as the characteristic orientation parameters of each model. These averaged orientation values are presented in Table 5 for clarity and comparison.

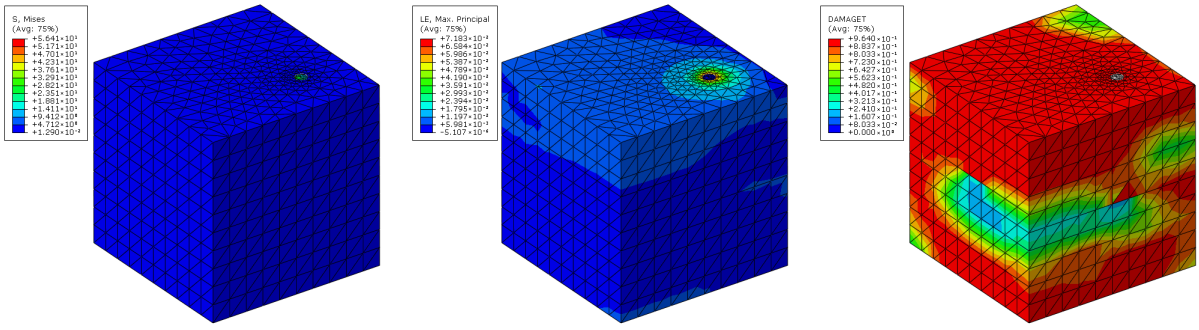
Table 5. Fiber orientation and model numbering.

θ	φ	Model ID	Group (θ)
7.77	236.74	1	
7.99	252.52	2	0–15
9.84	187.79	3	
23.59	223.30	4	
18.74	169.23	5	15–30
20.84	157.28	6	
39.91	128.49	7	
36.21	224.04	8	30–45
35.79	103.56	9	
51.86	204.51	10	
53.99	188.83	11	45–60
49.23	265.25	12	
68.14	293.42	13	
69.44	168.19	14	60–75
66.48	185.38	15	
84.02	191.72	16	
84.02	219.27	17	75–90
80.06	159.55	18	

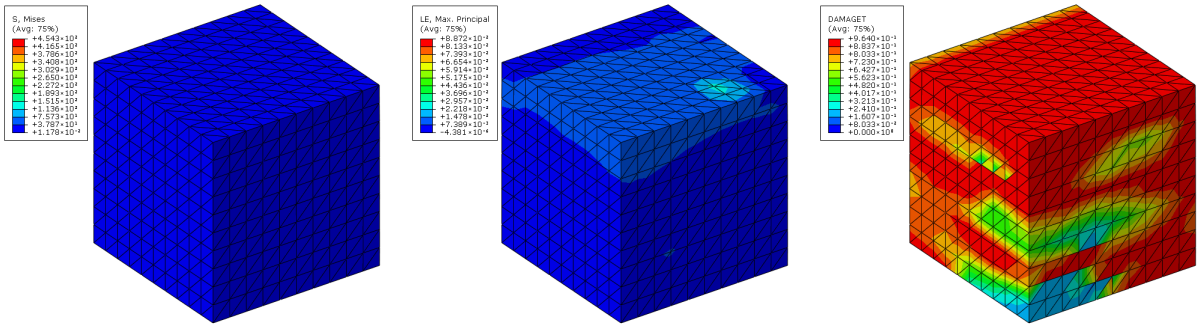
As shown in Figures 19–21, the parameter θ has a significant influence on the tensile strength of the specimen: the overall tensile capacity decreases as θ increases. Similarly, an increase in φ also leads to a reduction in tensile strength under the same loading conditions. Moreover, the tensile strengths of all models with different orientation angles are lower than that of the reference model, as shown in Figure 9.



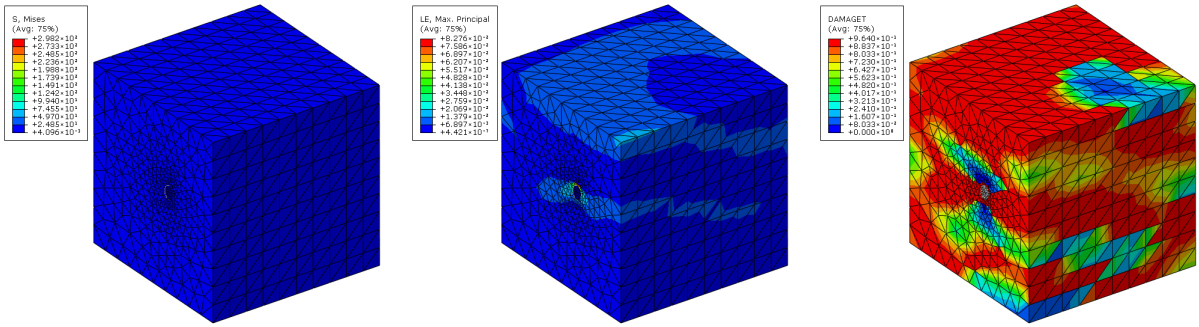
(**a**) The fiber orientation angle range is 0–15 degrees.



(**b**) The fiber orientation angle range is 15–30 degrees.

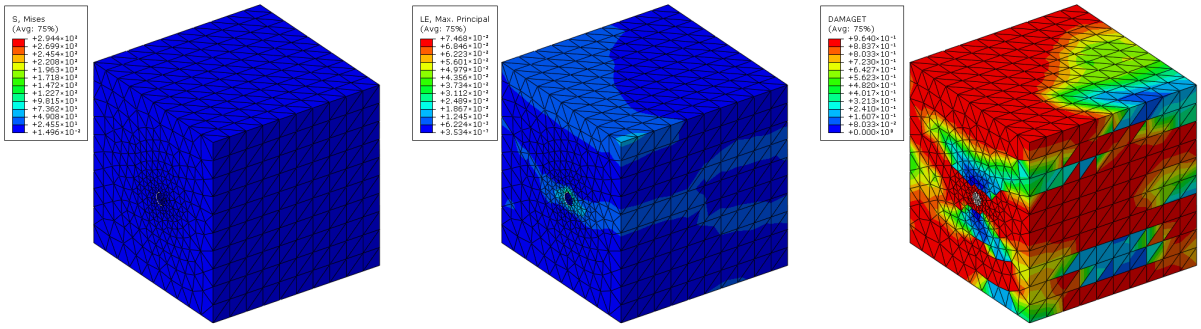


(**c**) The fiber orientation angle range is 30–45 degrees.

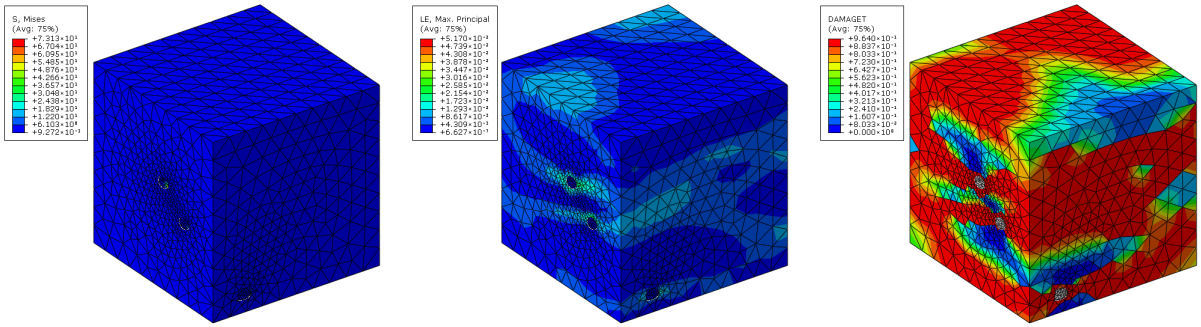


(**d**) The fiber orientation angle range is 45–60 degrees.

Figure 19. *Cont.*



(**e**) The fiber orientation angle range is 60–75 degrees.



(**f**) The fiber orientation angle range is 75–90 degrees.

Figure 19. von Mises stress, maximum principal strain, and damage of models with different fiber orientations.

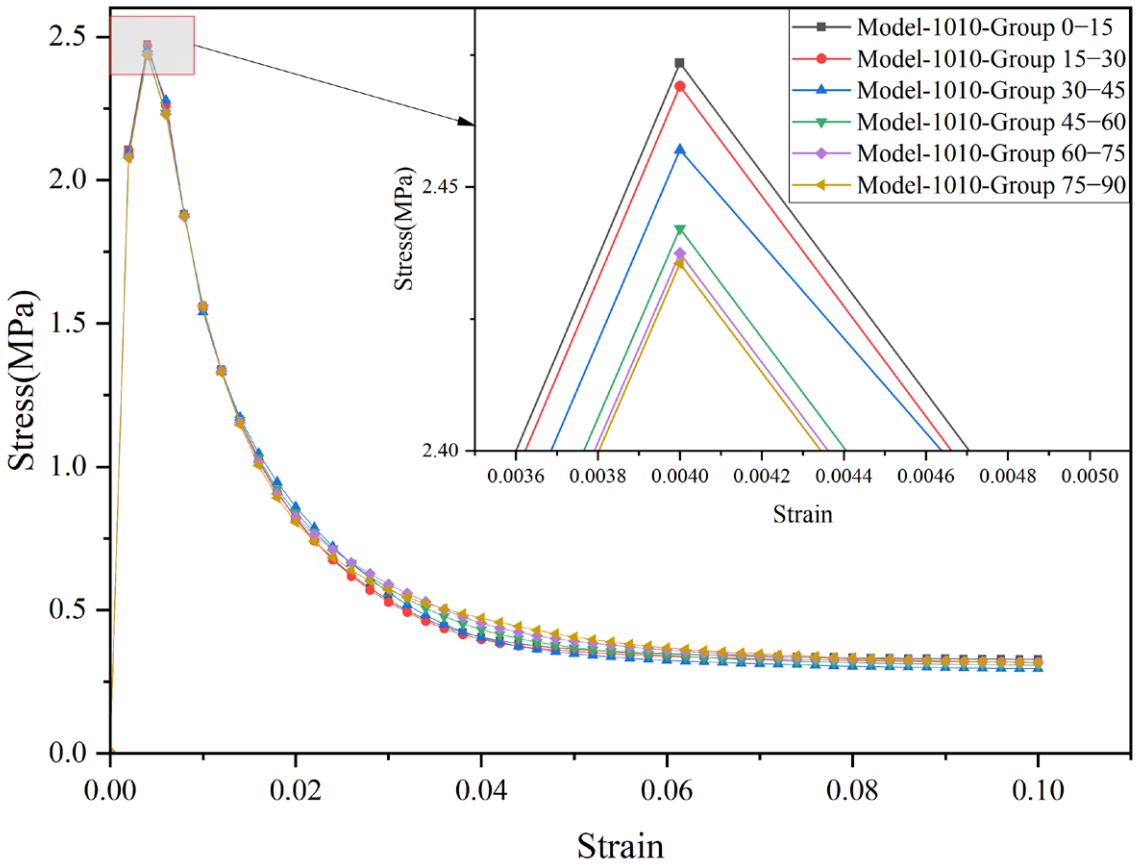


Figure 20. Stress–strain curves of models with different orientations of fibers.

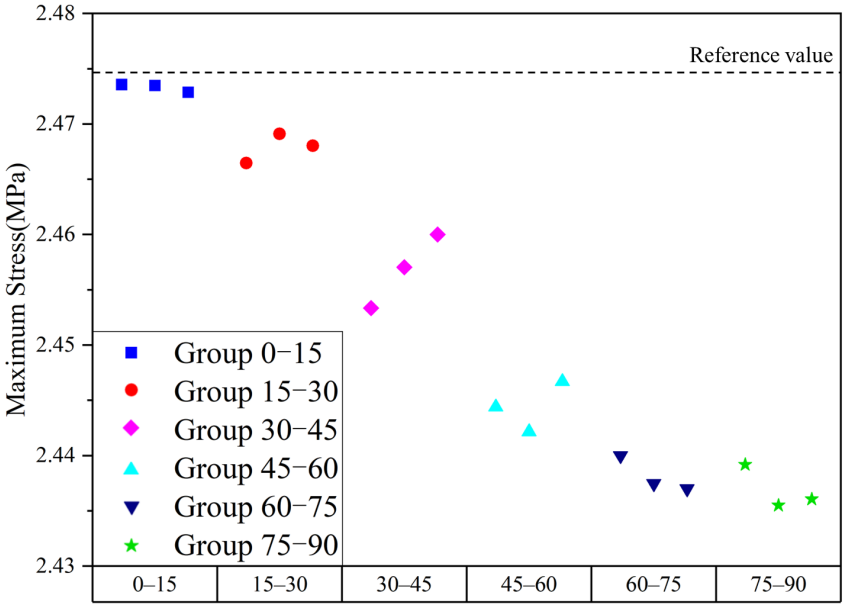


Figure 21. Variation in the maximum stress with changing fiber orientation angle.

When the fiber orientation angle is large, the fibers deviate further from the positive *z*-axis, resulting in a reduced axial component of the tensile load carried by the fibers and, consequently, a significant decrease in their axial load-bearing capacity. In this situation, the external load direction is misaligned with the fiber axis, preventing the fibers from effectively sustaining shear stress. The local stress is therefore transferred as interfacial shear stress along the fiber–matrix interface. A portion of the tensile capacity thus relies on cohesive bonding at the fiber–matrix interface; once the load continues to increase and interfacial debonding occurs, the overall tensile strength of the material decreases sharply. The relevant figures are shown in Figures 22–24.

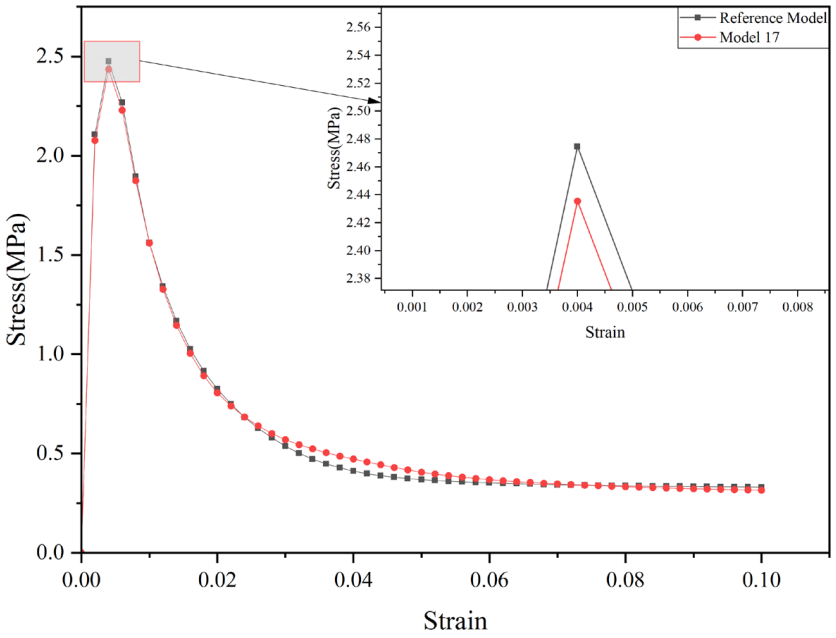


Figure 22. Comparison of the maximum stress between Model 17 and the reference model.

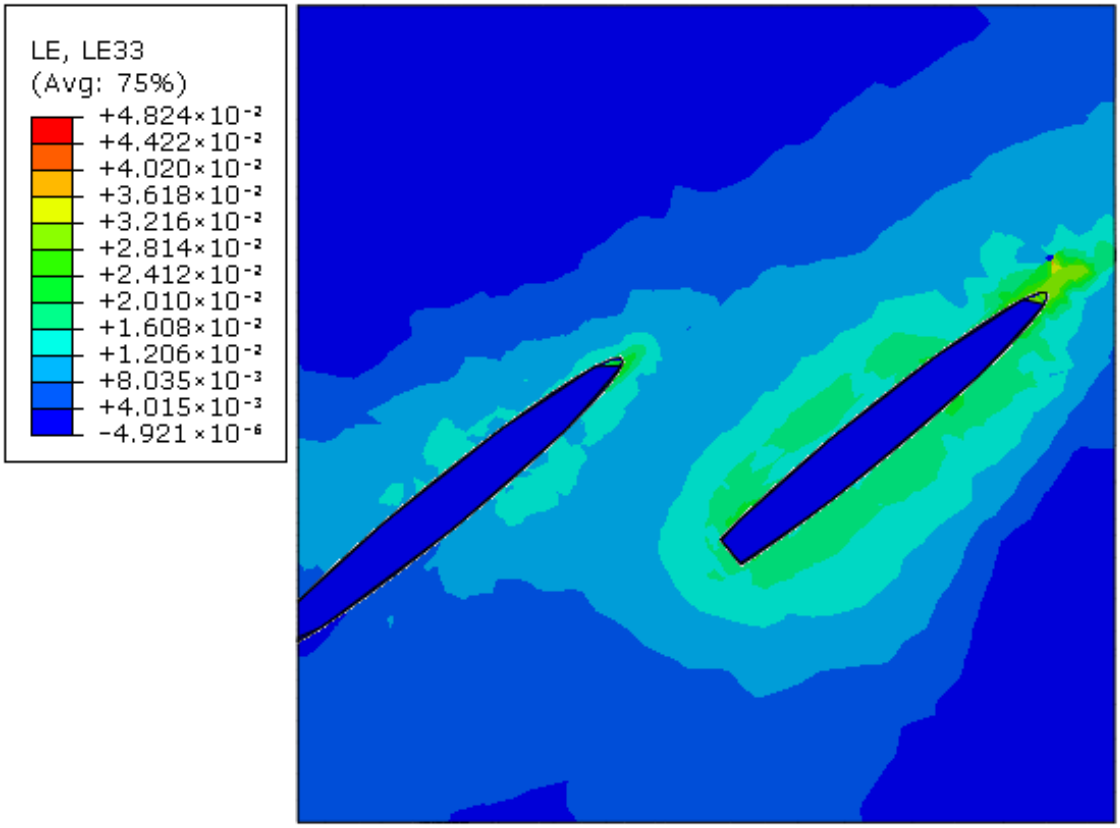


Figure 23. Z-axis section view of the strain field in the z-direction of Model 17.

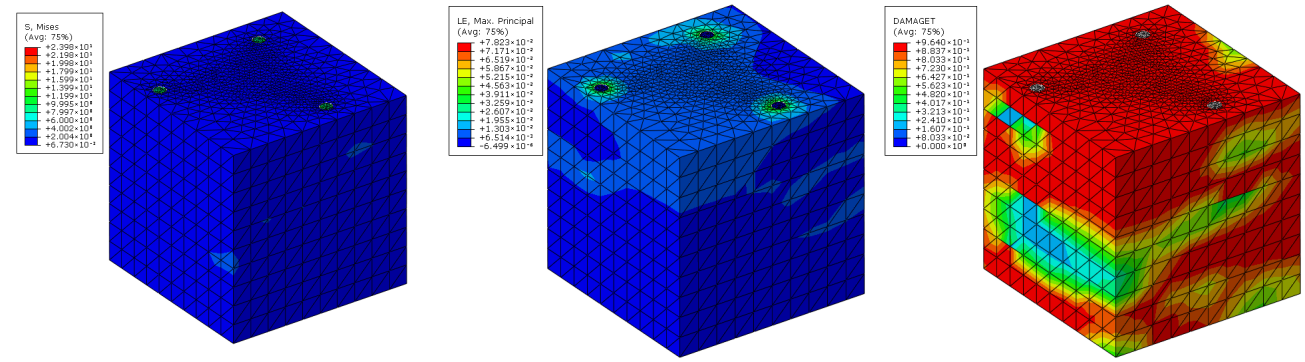


(**a**) (**b**)

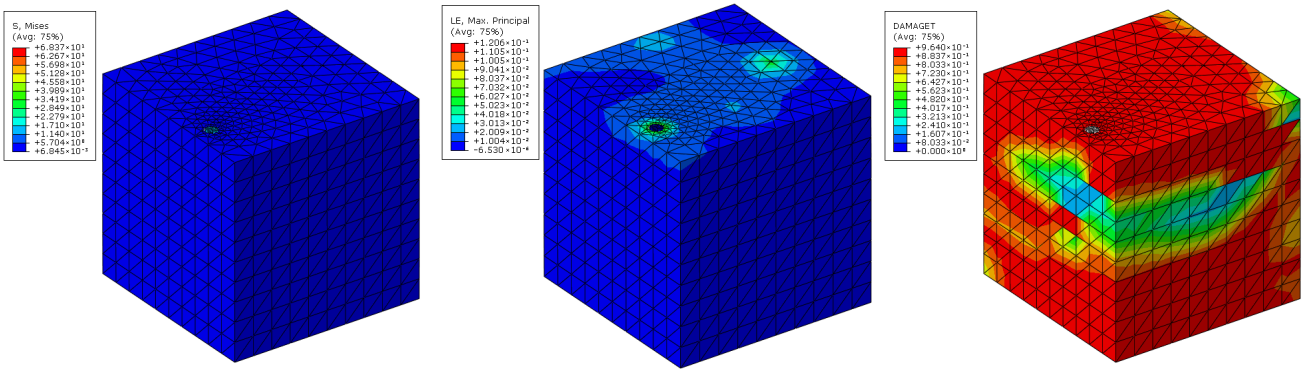
Figure 24. (**a**,**b**) Debonding phenomenon that occurred on the surface of Model 17.

5.5. Effect of Spatial Fiber Distribution on the Macroscopic Mechanical Behavior

As shown in Figures 25–27, the model exhibiting the highest stress (Model-1025, representing the model's eigenvalue value as 1025) and the one exhibiting the lowest stress (Model-1014, representing the model's eigenvalue value as 1014) are selected and compared with the reference model (Model-1010). From the *z*-axis views, it can be observed that the spatial fiber distributions in Model-1014 and Model-1025 are both more uniform than that in Model-1010. From the *x*-axis views, it is found that due to random fiber placement, Model-1014 contains four fibers truncated by the cube boundaries, Model-1025 has one truncated fiber, and the reference model Model-1010 has two.



(**a**) Model with eigenvalue of 1014 (Model-1014).



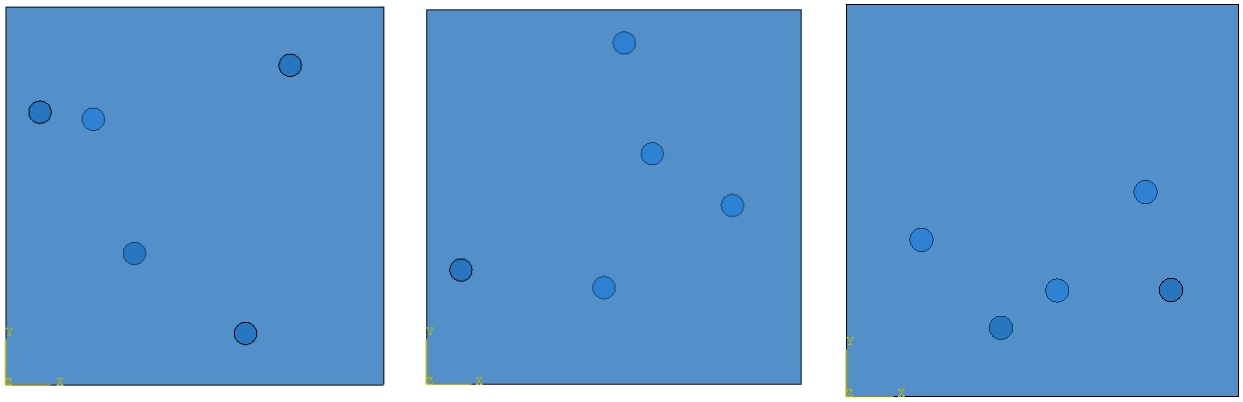
(**b**) Model with eigenvalue of 1025 (Model-1025).

Figure 25. von Mises stress, maximum principal strain, and damage of models with different spatial distributions.

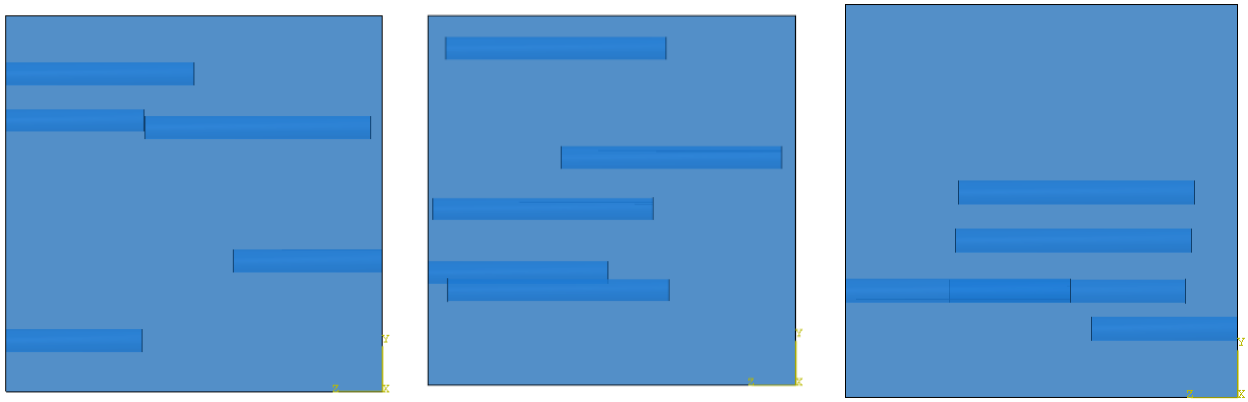


Figure 26. Variation in the maximum stress under different spatial fiber distributions.

These observations indicate that variations in the spatial fiber distribution within the specimen lead to only minor fluctuations in the overall tensile strength. The primary factor governing tensile performance is the steel-phase volume fraction, which is consistent with the results obtained in the preceding simulations.



(**a**) Z-axis views of Models 1014, 1025, and 1010



(**b**) X-axis views of Models 1014, 1025, and 1010

Figure 27. Oblique views of Models 1014, 1025, and 1010.

6. Conclusions

By systematically varying five microscopic morphological parameters, we studied fiber influences on the macroscopic mechanical behavior of fiber-reinforced concrete and analyzed their influence levels. The use of the control variable method enables a precise identification of the correlation between macroscopic mechanical properties and microscopic structural features. In addition, by considering fiber–matrix cohesive interfaces, damage parameters, and calibrated CDP parameters, the simulation presents a strong case for closely representing actual engineering behavior. This provides a meaningful reference for mechanical performance prediction, which can be widely applied in practical structural applications.

The main findings are as follows:

(1) The fiber reinforcement effect exhibits an optimal range governed by the fiber quantity, size, and distribution. Moderate increases in fiber number or diameter/length enhance tensile strength, whereas an excessive fiber content or oversized fibers reduce the minimum matrix ligament, trigger premature interfacial debonding, and diminish strengthening efficiency, even leading to a decrease in the initial Young's modulus. A critical fiber length (l_c) also exists: fibers shorter than l_c contribute weakly, while those exceeding l_c provide pronounced strengthening.

(2) The macroscopic stiffness is dictated by the effective load-bearing contribution of fibers, while interfacial damage, fiber clustering, and end-induced shear stresses dominate the interfacial stress transfer mechanism. The initial Young's modulus shows a non-monotonic dependence on the fiber number or diameter, reflecting whether fibers can cooperate with the matrix during early deformation. Orientation deviations

from the tensile axis reduce shear-carrying efficiency and axial reinforcement, and an uneven spatial distribution or premature debonding interrupts stress transfer continuity, causing stiffness reduction or fluctuations.

(3) The fiber orientation and spatial distribution both affect the ultimate load-bearing capacity, with orientation-induced randomness exerting a more pronounced influence and spatial distribution playing a comparatively minor role. Larger deviations from the tensile direction markedly reduce axial load-bearing efficiency, while variations in spatial distribution at identical steel volume fractions cause only limited strength fluctuations, confirming that the steel-phase volume fraction is the primary factor governing the macroscopic load capacity.

7. Future Prospects

The proposed stochastic RVE framework can be further developed by coupling it with multi-scale structural analyses, performing experimental calibration for different fiber types, and testing extended damage mechanisms such as fatigue, freeze–thaw, and high-temperature exposure. In the longer term, numerical databases generated from random fiber configurations may also support surrogate or machine learning models for rapid design optimization of fiber-reinforced concrete.

From a practical perspective, the present results are particularly relevant for the performance-based design of fiber-reinforced tunnel linings, precast segments, industrial floors, pavements, bridge decks, and shotcrete linings, where steel fibers are increasingly used to enhance the tensile capacity and for crack control. The identified relationships between fiber parameters and macroscopic stiffness and strength can help engineers select an appropriate fiber content and improve construction procedures to achieve a more reliable structural performance.

Author Contributions: Conceptualization, Y.S.; Methodology, S.X., Z.Z., J.Y. and Y.S.; Software, S.X. and Y.S.; Validation, S.X.; Investigation, S.X. and Z.Z.; Writing—original draft, S.X.; Writing—review & editing, Z.Z., J.Y. and Y.S.; Visualization, S.X.; Supervision, J.Y.; Project administration, Y.S.; Funding acquisition, Y.S. All authors have read and agreed to the published version of the manuscript.

Funding: This work was supported by the National Natural Science Foundation of China (No. 52505158), the Qin Chuang Yuan high-level innovation and entrepreneurship talent project (No. QCYRCXM-2022-306), and the Shock and Vibration of Engineering Materials and Structures Key Laboratory of Sichuan Province (No. 22kfgk04).

Institutional Review Board Statement: Not applicable.

Informed Consent Statement: Not applicable.

Data Availability Statement: The data presented in this study are available on request from the corresponding author (for model and code privacy reasons).

Conflicts of Interest: The authors declare no conflict of interest.

References

1. Ravikumar, C.S.; Ramasamy, V.; Thandavamoorthy, T.S. Effect of fibers in concrete composites. *Int. J. Appl. Eng. Res.* **2015**, *10*, 419–430.
2. Paul, S.C.; van Zijl, G.P.A.G.; Šavija, B. Effect of fibers on durability of concrete: A practical review. *Materials* **2020**, *13*, 4562. [CrossRef]
3. Afroughsabet, V.; Biolzi, L.; Ozbakkaloglu, T. High-performance fiber-reinforced concrete: A review. *J. Mater. Sci.* **2016**, *51*, 6517–6551. [CrossRef]
4. Behbahani, H.; Nematollahi, B.; Farasatpour, M. Steel fiber reinforced concrete: A review. In Proceedings of the International Conference on Structural Engineering Construction and Management (ICSECM2011), Kandy, Sri Lanka, 15–17 December 2011; pp. 1–12.

5. Azandariani, M.G.; Vajdian, M.; Asghari, K.; Mehrabi, S. Mechanical properties of polyolefin and polypropylene fibers-reinforced concrete—An experimental study. *Compos. Part C Open Access* **2023**, *12*, 100410. [CrossRef]
6. Chen, Y.; Waheed, M.S.; Iqbal, S.; Rizwan, M.; Room, S. Durability properties of macro-polypropylene fiber reinforced self-compacting concrete. *Materials* **2024**, *17*, 284. [CrossRef]
7. Abousnina, R.; Premasiri, S.; Anise, V.; Lokuge, W.; Vimonsatit, V.; Ferdous, W.; Alajarmeh, O. Mechanical properties of macro polypropylene fibre-reinforced concrete. *Polymers* **2021**, *13*, 4112. [CrossRef]
8. Abdulkareem, O.M.; Guneyisi, E.; Boubekra, N. Durability of polypropylene fiber reinforced concrete—A review. *Electron. J. Struct. Eng.* **2022**, *22*, 1–20. [CrossRef]
9. Li, Y.; Gu, Z.; Zhao, B.; Zhang, J.; Zou, X. Experimental study on mechanical and durability properties of basalt fiber reinforced concrete under freeze–thaw cycles. *Materials* **2022**, *15*, 1052.
10. Yang, W.; Liu, H.; Wang, H. Experimental study on mechanical properties of basalt fiber reinforced nano-SiO_2 concrete after high temperature. *Front. Mater.* **2024**, *11*, 1415144. [CrossRef]
11. Yang, X.; Wang, Z.; Wang, X. Study on mechanical properties of nano-TiC- and nano-SiO_2-modified basalt fiber concrete. *Buildings* **2024**, *14*, 2120. [CrossRef]
12. Zhao, L.; Chen, G.; Zhang, Y.; Zhu, H.; Zhao, H.; Tang, J.; Yuan, J. Mechanical properties of hybrid fibers and nano-silica reinforced concrete. *Structures* **2024**, *55*, 106843.
13. Fode, T.A.; Jande, Y.A.C.; Kivevele, T. Physical, mechanical, and durability properties of concrete incorporating waste synthetic fibers for green environment—A critical review. *Heliyon* **2024**, *10*, e25936. [CrossRef] [PubMed]
14. Anish, V.; Logeshwari, J. A review on ultra high-performance fibre-reinforced concrete: Properties and applications. *J. Eng. Appl. Sci.* **2024**, *71*, 357. [CrossRef]
15. Li, Y.; Ruan, X.; Akiyama, M.; Zhang, M.; Xin, J.; Lim, S. Modelling method of fibre distribution in steel fibre reinforced concrete based on X-ray image recognition. *Compos. Part B Eng.* **2021**, *223*, 109124. [CrossRef]
16. Naderi, S.; Rahmani, A.; Simms, K. A novel framework for modelling the 3D mesostructure of steel fibre reinforced concrete. *Constr. Build. Mater.* **2020**, *261*, 120013. [CrossRef]
17. Khalel, H.H.Z.; Khan, M. Modelling fibre-reinforced concrete for predicting optimal mechanical properties. *Materials* **2023**, *16*, 3700. [CrossRef]
18. Sun, W.; Zhang, W.; Yuan, J.; Gao, X.; Wu, Y.; Ni, W.; Feng, J. Multi-scale study on penetration performance of steel fiber reinforced ultra-high performance concrete. *Constr. Build. Mater.* **2024**, *417*, 135930. [CrossRef]
19. Shams, M.A.; El-Hafidi, A.; Benjeddou, O. Fracture analysis of steel fibre-reinforced concrete using finite element method modeling. *Front. Mater.* **2024**, *11*, 1355351. [CrossRef]
20. Kozák, V.; Vala, J. Use of cohesive approaches for modelling critical states in fibre-reinforced structural materials. *Materials* **2024**, *17*, 3177. [CrossRef] [PubMed]
21. Bordelon, A.C.; Roesler, J.R. Spatial distribution of synthetic fibers in concrete with X-ray computed tomography. *Cem. Concr. Compos.* **2014**, *53*, 35–43. [CrossRef]
22. Han, J.; Zhao, M.; Chen, J.; Lan, X. Effects of steel fiber length and coarse aggregate maximum size on mechanical properties of steel fiber reinforced concrete. *Constr. Build. Mater.* **2019**, *209*, 577–591. [CrossRef]
23. Li, B.; Xu, L.; Shi, Y.; Chi, Y.; Liu, Q.; Li, C. Effects of fiber type, volume fraction and aspect ratio on the flexural and acoustic emission behaviors of steel fiber reinforced concrete. *Constr. Build. Mater.* **2018**, *181*, 474–486. [CrossRef]
24. Soroushian, P.; Lee, C.D. Distribution and orientation of fibers in steel fiber reinforced concrete. *Mater. J.* **1990**, *87*, 433–439.
25. D'Antino, T.; Colombi, P.; Carloni, C.; Sneed, L.H. Estimation of a matrix-fiber interface cohesive material law in FRCM-concrete joints. *Compos. Struct.* **2018**, *193*, 103–112. [CrossRef]
26. Amin, A.; Foster, S.J. Numerical modelling of large-scale steel fibre reinforced concrete beams failing in shear. *Eng. Struct.* **2014**, *79*, 54–67.
27. Blagojević, P.; Blagojević, N.; Kukaras, D. Flexural behavior of steel fiber reinforced concrete beams: Probabilistic numerical modeling and sensitivity analysis. *Appl. Sci.* **2021**, *11*, 9792. [CrossRef]
28. Shakor, P.; Nejadi, S. Finite element modelling of steel fibre reinforced concrete using the concrete damage plasticity model. *Comput. Concr.* **2017**, *19*, 643–654.
29. Farsi, A.; Bedi, A.; Latham, J.P.; Bowers, K. Simulation of fracture propagation in fibre-reinforced concrete using FDEM: An application to tunnel linings. *Comput. Mech.* **2020**, *65*, 1357–1373. [CrossRef]
30. Landović, A.; Čeh, A.; Starčev-Ćurčin, A.; Šešlija, M. Small-Scale and Large-Scale Modeling of Fiber-Reinforced Concrete Girders. *Buildings* **2024**, *14*, 3812. [CrossRef]
31. Michał, S.; Andrzej, W. Calibration of the CDP model parameters in Abaqus. In Proceedings of the 2015 World Congress on Advances in Structural Engineering and Mechanics (ASEM 15), Incheon, Republic of Korea, 25–29 August 2015.
32. Naderi, S.; Zhang, M. 3D meso-scale modelling of tensile and compressive fracture behaviour of steel fibre reinforced concrete. *Compos. Struct.* **2022**, *291*, 115690. [CrossRef]

33. Li, Z.; Wu, M.; Wu, J.; Cui, Y.; Xue, X. Steel Fibre Reinforced Concrete Meso-Scale Numerical Analysis. *Adv. Civ. Eng.* **2020**, *2020*, 2084646. [CrossRef]
34. Soe, K.T.; Zhang, Y.X.; Zhang, L.C. Impact resistance of hybrid-fiber engineered cementitious composite panels. *Compos Struct* **2013**, *104*, 320. [CrossRef]
35. Musmar, M. Tensile strength of steel fibre reinforced concrete. *Contemporary Eng. Sci.* **2013**, *6*, 225–237. [CrossRef]
36. Ling, S.; Chengbin, D.; Yafeng, Y.; Yongheng, L. Analysis and prediction of compressive and split-tensile strength of secondary steel fiber reinforced concrete based on RBF fuzzy neural network model. *PLoS ONE* **2024**, *19*, e0299149. [CrossRef]
37. Freire Rodrigues, T.L.; Durand, R. Numerical modeling of steel fiber reinforced concrete using cohesive elements. *J. Build. Pathol. Rehabil.* **2023**, *8*, 69. [CrossRef]
38. George, J.; Rama, J.K.; Kumar, M.S.; Vasan, A. Behavior of plain concrete beam subjected to three point bending using concrete damaged plasticity (CDP) model. *Mater. Today Proc.* **2017**, *4*, 9742–9746. [CrossRef]
39. Stukhlyak, P.D.; Buketov, A.V.; Panin, S.V.; Maruschak, P.O.; Moroz, K.M.; Poltaranin, M.A.; Vukherer, T.; Kornienko, L.A.; Lyukshin, B.A. Structural fracture scales in shock-loaded epoxy composites. *Phys. Mesomech.* **2015**, *18*, 58–74. [CrossRef]
40. Chen, M.; De Corte, W.; Zhang, F.; Taerwe, L. Parametric Analysis of CDP Modeling of High-Strength Concrete in Abaqus to Study the Direct-Shear Behavior of Joints in Precast Concrete Segmental Bridges. In Proceedings of the International Conference on Engineering Structures, Guangzhou, China, 8–11 November 2024; Springer: Singapore, 2024; pp. 318–328.
41. Hu, A.; Du, X.; Wang, F.; Li, J.; Zhang, T.; Li, Y. Study on Damage Mechanism of Fiber Concrete with Initial Pores. *Materials* **2025**, *18*, 916. [CrossRef]
42. Van der Aa, P.J. *Biaxial Stresses in Steel Fibre Reinforced Concrete Modelling the Pull Out-Behaviour of a Single Steel Fibre Using FEM*; Einhoven University of Technology: Eindhoven, The Netherlands, 2014.
43. Abbas, Y.M. Microscale cohesive-friction-based finite element model for the crack opening mechanism of hooked-end steel fiber-reinforced concrete. *Materials* **2021**, *14*, 669. [CrossRef]
44. Rilem Tc 162-Tdf. Test and design methods for steel fibre reinforced concrete: Uni-axial tension test for steel fibre reinforced concrete. *Mater. Struct.* **2001**, *34*, 3–6. [CrossRef]
45. Luo, Z.; Li, X.; Zhao, F. Complete splitting process of steel fiber reinforced concrete at intermediate strain rate. *J. Cent. South Univ. Technol.* **2008**, *15*, 569–573. [CrossRef]

Disclaimer/Publisher's Note: The statements, opinions and data contained in all publications are solely those of the individual author(s) and contributor(s) and not of MDPI and/or the editor(s). MDPI and/or the editor(s) disclaim responsibility for any injury to people or property resulting from any ideas, methods, instructions or products referred to in the content.